A micromechanical model for the determination of nonlinear coupled electro-magneto-thermo-elastic effects on magnetoelectric composites

Ziwei Li[a], Junjie Ye[a*], Lu Liu[a], Yiwei Wang[a], Yang Li[b], Yang Shi[a], Dianzi Liu [c*]

[a] Joint Laboratory of International Cooperation on Structural Mechanics of Composite Materials for Electronic Devices, Ministry of Education of China, Xidian University, Xi'an 710071, China

[b] Xi'an Institute of Space Radio Technology, Xi'an 70100, China

[c] School of engineering, Mathematica and physics, University of east Anglia, Norwich UK NR4 7TJ

Abstract:

Magnetoelectric (ME) composites composed of piezoelectric and magnetostrictive materials have excellent energy conversion properties. In this paper, a novel micromechanical modeling framework is proposed to study the effective material properties and nonlinear electro-magneto-elastic behaviors of magnetoelectric composites under multiple physical fields. Initially, a fully coupled nonlinear electro-magneto-thermo-elastic constitutive relationship is established. Based on finite volume direct averaging micromechanics (FVDAM), the local stress, electric displacement and magnetic flux density distribution of discrete elements are obtained by constructing the generalized local stiffness matrix and assembling the global stiffness matrix. The equivalent material coefficients of the magnetoelectric composite are obtained by employing the homogenization technique. Results of the numerical model are compared with different discrete elements and experimental data to verify the convergence and effectiveness of the developed algorithm. Moreover, effects of external prestress, ambient temperature, microscopic structure and applied magnetic field intensity on material properties such as magnetoelectric and piezomagnetic coefficients are investigated. Finally, the influences of initial damage and constituent phase volume fraction on the equivalent material coefficient and local mechanical response are discussed. The promising results provide a solid foundation for theoretical study and useful insight into the optimal design of high-performance ME composites.

Keywords: Magnetoelectric effect, Finite volume method, Nonlinear coupling behavior, Parametric micromechanical model

1. Introduction

Magneto-electric (ME) composites composed of piezoelectric and magnetostrictive materials are widely used in emerging intelligent equipment and devices, owing to their mechanical-electric-magnetic coupling characteristics [1–4]. As compared to single crystal ferroelectric materials, ME composites including piezoelectric materials as the matrix exhibit significant advantages in material ductility, excellent plasticity and structural integrity [5,6], thus attracting extensive attention in the fields of bionic robots and structural health monitoring. Manufacturing the intelligent devices composed of ME composites aims at high sensitivity, lightweight, and low pollution, therefore the optimization of ME composites is necessary to meet the growing demands of smart devices [7–9]. However, the combination of different components and the multi-field coupling characteristics leads to additional complexity in the analysis of interaction and structural integrity. Thus, both the

*Corresponding authors.
Email address: ronkey6000@sina.com (Junjie Ye)
dianzi.liu@uea.ac.uk (Dainzi Liu)

effective coefficients and the local microscopic response of the composite materials need to be considered to achieve the accurate analysis.

In general, the composition of ME composites can be divided into two constituent phases, which include a magnetostrictive phase (such as Nickel, or Terfenol- D) and piezoelectric phase (such as polyvinylidene fluoride (PVDF) or lead zirconate titanate (PZT)) [10,11]. One of the most important characteristics of ME composites is the magneto-mechanical-electric conversion property, that is, the ME coupling effect that cannot be observed in single ferroelectric or ferromagnetic materials. This ME coupling effect is demonstrated by the induced magnetization under the external electric field through the magnetostriction effect, or the polarization caused by the external magnetic field via the electromechanical effect [12,13]. Therefore, the research of ME composite requires the mechanical-electric-magnetic coupling analysis of piezoelectric characteristic, magnetostrictive characteristic and thermoelastic effects, as shown in Fig. 1. In the past decades, several analytical and numerical techniques have been developed to predict the effective material properties and coupling effects [14,15] of ME composites in order to avoid the time-consuming and laborious experimental measurement. As magnetostrictive materials, such as Terfenol-D, exhibit nonlinear mechanical behaviors in complex multi-field environments [16,17], it is extremely significant to construct a numerical model that includes nonlinear constitutive relationships to predict the nonlinear magnetoelectric response of ME composites. Taking the benefit from the advance in classical mechanics theory and experimental tests, the magnetostrictive nonlinear constitutive model has been well established. By comparing numerical results with experimental data, Carmen and Mitrovic [18] proposed a standard square model. Duenas et al. [19] proposed an analytical model that used magnetization instead of magnetic field intensity as the independent variable in the calculation of the effective magnetostrictive characteristics. Based on the Gibbs free energy theory, Zheng and Liu [20,21] established a general nonlinear constitutive equation suitable for the complex multi-field coupling analysis and proposed the corresponding analytical expression.

In order to reveal and analyze the effects of the volume fraction ratio, material distribution and microstructure on the macroscopic material properties, it is necessary to develop parametric modeling techniques for ME composites, therefore realizing the actual material preparation by numerical simulations. Early modeling techniques were based on classical micromechanical models. For example, Dinzart et al. [22] constructed the Mori-Tanaka (MT) model to study the coating inclusion problem arising from the analysis of ME composites. Herbst et al. [23] established the Composite Sphere Assemblage (CSA) model for particulate inclusion in ME composites, and Tong et al. [24] developed the Generalized Self-consistent Method (GSCM) for interface layer properties of fiber-reinforced ME composites. The above classical micromechanical models provide explicit analytical expressions and can obtain effective properties. However, the classical micromechanical model exists shortcomings, specifically manifested in the following aspects: 1) The classical microscopic mechanics model ignores the internal interaction of composites, leading to an ineffective analysis of interface damage, delamination, and porosity defects. 2) There is no effective parametric modeling, resulting in an inability to predict the local mechanical responses at the microscopic scale. The local stress distribution serves as a crucial indicator for microcrack and damage initiation, necessitating the advance in computational models with complex boundary conditions. At present, the finite element method (FEM) is widely used to construct micromechanical models, considering its concise theoretical framework and the capability of simulating intricate shapes and arrangements at the microstructure scale. Malakooti [25], Sladek

[26] and Govorukha [27] employed the FEM technique to investigate the electro-mechanical coupling characteristics of piezoelectric composites. Wang and Zhang et al. [28,29] implemented the nonlinear magnetostrictive constitutive relationship into the finite element model to study the effects of the magnetic field intensity and frequency on the magnetoelectric coupling performance. Utilizing Gaussian numerical integration points, the aforementioned FEM models can be developed to assess the mechanical response and electromagnetic field distribution in various directions at each element [30]. However, a substantial number of integral points are essential to ensure sufficient accuracy during the homogenization process using FEM. Therefore, it is demanding to establish the nonlinear constitutive model of the material coefficients in use of iterative algorithms for guaranteeing the computational convergence.

To achieve this goal, the finite volume mechanics method is used to construct a micromechanical model with coupling characteristics of the multi-physics field. Initially, finite volume mechanics techniques were primarily employed in the field of fluid mechanics, while Pindera et al. [31,32] introduced solid mechanics as a numerical approach for investigating the micromechanical behavior of periodic composites. Khatam [33] and Cavalcante [34] further enhanced the accuracy of method by incorporating parametric elements for discretizing the model. Compared with traditional analysis methods, the distinctive feature of FVDAM is that it provides an explicit analytical expression of the local stiffness matrix for each discrete element in the local region. In addition, FVDAM uses the average surface quantity as the basic unknown variable to construct the global stiffness matrix, rather than using the unknown quantity at Gaussian points. In the existing research, it has been proved that the computational efficiency of the FVDAM model is higher and has sufficient accuracy compared with other numerical models [35–37]. Li et al. [38,39] have already utilized the finite volume theory to build effective microscopic mechanical models for piezoelectric composite materials and magnetostrictive composite materials, respectively. However, the FVDAM theory has not yet achieved the study of nonlinear ME effects in an electro-magnetic-mechanical environment with full coupling in the literature.

Stemming from the theoretical framework of FVDAM, this paper has developed a microscopic modelling framework that can effectively predict the nonlinear mechanical behaviors of ME composites. On this basis, the local response and equivalent material properties are obtained under the consideration of external multi-physics fields and internal microstructure. The subsequent sections present the remaining parts of this paper as follows: Section 2 describes the construction process of nonlinear coupled electro-magneto-thermo-elastic constitutive equations. The Section 3 derives the generalized numerical solution using the finite volume theory and constructs the parameterized micromechanical model of the FVDAM. As compared with the experimental results, the validity of the numerical model results is conducted in Section 4. Then, the convergence of the model is demonstrated by the local field distributions of the mechanical model with different mesh densities. Subsequently, the influence of magnetic field intensity, prestress and temperature on magnetostrictive strain, electric field intensity and ME coupling coefficients are discussed in detail. Finally, the results of stress distribution and equivalent material properties under the influence of initial damage with the variation of magnetostrictive phase volume fraction are obtained. This research is summarized in Section 5.

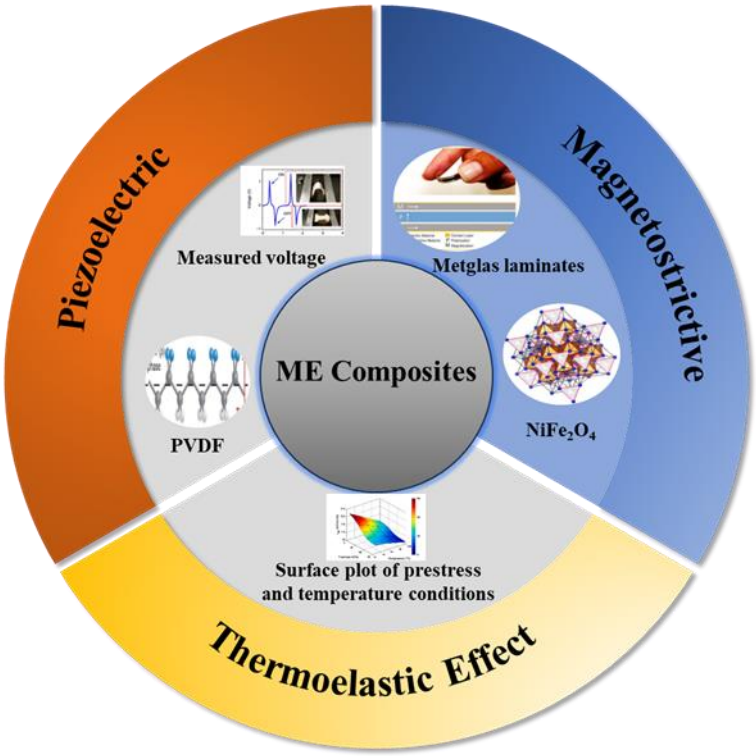

Fig. 1. Surface plot of compressive prestress and temperature conditions [45]. Properties and application of each component phase material of magnetoelectric composites. Structural configuration of PVDF and its copolymers [46]. Measured voltage response of an array of PVDF-TrFE fibers under cycling bending at 1 Hz [47]. Schematic of the crystal structure of NiFe2O4 NPs [48]. Digital photograph and schematic presentation of ME laminate composites [49].

2. Electro-Magneto-Thermo-Elastic coupling constitutive relation

For stationary behavior without external electric field or physical forces, linear fully coupled electro-magneto-thermo-elastic constitutive relation consists of divergence equations (i.e., elastic equilibrium and Gauss's law) and gradient equations (for example, strain-displacement, electric field-potential and magnetic field-potential relations). This constitutive relation can be described by generalized Hooke's law [40]:

$$\sigma_{ij} = C_{ijkl}\varepsilon_{kl} - e_{kij}E_k - q_{kij}H_k - \Lambda_{ij}\Delta T \tag{1}$$

$$D_i = e_{ikl}\varepsilon_{kl} + \kappa_{ik}E_k + \alpha_{ik}H_k + \rho_i\Delta T \tag{2}$$

$$B_i = q_{ikl}\varepsilon_{kl} + \alpha_{ik}E_k + \mu_{ik}H_k + \lambda_i\Delta T \tag{3}$$

where σ_{ij}, D_i and B_i are stress, electric displacement and magnetic flux density components, respectively. C_{ijkl}, e_{kij}, q_{kij}, κ_{ik}, α_{ik} and μ_{ik} denote the elastic stiffness, piezoelectric, piezomagnetic, dielectric permittivity, magnetoelectric and magnetic permeability coefficients, respectively. Λ_{ij}, ρ_i and λ_i represent the thermal stress, pyroelectric and pyromagnetic

coefficients, respectively. To facilitate the calculation, the constitutive relations in Eqs. (1)-(3) are written in a matrix form as follows:

$$\mathbf{Y} = \mathbf{G}\mathbf{X} - \mathbf{\Gamma}\Delta T \tag{4}$$

where the vectors $\mathbf{X}$ and $\mathbf{Y}$ are formulated as:

$$\mathbf{X} = \left[\varepsilon_{11},\ \varepsilon_{22},\ \varepsilon_{33},\ 2\varepsilon_{23},\ 2\varepsilon_{13},\ 2\varepsilon_{12},\ -E_1,\ -E_2,\ -E_3,\ -H_1,\ -H_2,\ -H_3\right] \tag{5}$$

$$\mathbf{Y} = \left[\sigma_{11},\ \sigma_{22},\ \sigma_{33},\ 2\sigma_{23},\ 2\sigma_{13},\ 2\sigma_{12},\ -D_1,\ -D_2,\ -D_3,\ -B_1,\ -B_2,\ -B_3\right] \tag{6}$$

and the symmetric coefficient matrix $\mathbf{G}$ and thermal coefficient vector $\mathbf{\Gamma}$ are defined as follows:

$$\mathbf{G} = \begin{bmatrix} \mathbf{C} & \mathbf{e}^{\mathbf{T}} & \mathbf{q}^{\mathbf{T}} \\ \mathbf{e} & -\boldsymbol{\kappa} & -\boldsymbol{\alpha} \\ \mathbf{q} & -\boldsymbol{\alpha} & -\boldsymbol{\mu} \end{bmatrix},\ \mathbf{\Gamma} = \begin{bmatrix} \mathbf{\Lambda} \\ \boldsymbol{\rho} \\ \boldsymbol{\lambda} \end{bmatrix} \tag{7}$$

In Eq. (7), the sixth-order square matrix $\mathbf{C}$ represents the elastic stiffness coefficients denoted by the contracted symbol. $\mathbf{e}^{\mathbf{T}}$ represents the transpose of the 3×6 rectangular matrix $\mathbf{e}$ that represents the corresponding piezoelectric coefficients. $\mathbf{q}^{\mathbf{T}}$ represents the transpose of the 3×6 rectangular matrix $\mathbf{q}$ that denotes the corresponding piezomagnetic coefficients. $\boldsymbol{\kappa}$ is a third-order square matrix corresponding to the dielectric permittivity coefficients, and $\boldsymbol{\mu}$ is a third-order square matrix corresponding to the magnetic permeability coefficients. $\boldsymbol{\alpha}$ is the third order square matrix representing the magnetoelectric coefficients. The sixth-order vector $\mathbf{\Lambda}$ denotes the thermal stress coefficients. The two third order $\boldsymbol{\rho}$ and $\boldsymbol{\lambda}$ denotes the corresponding pyroelectric coefficients and pyromagnetic coefficients. Therefore, the items in the fully coupled electro-magneto-thermo-elastic constitutive relation matrix shown in Eq. (7) are given as:

$$\mathbf{G} = \begin{bmatrix} C_{11} & C_{12} & C_{13} & C_{14} & C_{15} & C_{16} & e_{11} & e_{21} & e_{31} & q_{11} & q_{21} & q_{31} \\ C_{21} & C_{22} & C_{23} & C_{24} & C_{25} & C_{26} & e_{12} & e_{22} & e_{32} & q_{12} & q_{22} & q_{32} \\ C_{31} & C_{32} & C_{33} & C_{34} & C_{35} & C_{36} & e_{13} & e_{23} & e_{33} & q_{13} & q_{23} & q_{33} \\ C_{41} & C_{42} & C_{43} & C_{44} & C_{45} & C_{46} & e_{14} & e_{24} & e_{34} & q_{14} & q_{24} & q_{34} \\ C_{51} & C_{52} & C_{53} & C_{54} & C_{55} & C_{56} & e_{15} & e_{25} & e_{35} & q_{15} & q_{25} & q_{35} \\ C_{61} & C_{62} & C_{63} & C_{64} & C_{65} & C_{66} & e_{16} & e_{26} & e_{36} & q_{16} & q_{26} & q_{36} \\ e_{11} & e_{12} & e_{13} & e_{14} & e_{15} & e_{16} & \kappa_{11} & \kappa_{12} & \kappa_{13} & \alpha_{11} & \alpha_{12} & \alpha_{13} \\ e_{21} & e_{22} & e_{23} & e_{24} & e_{25} & e_{26} & \kappa_{21} & \kappa_{22} & \kappa_{23} & \alpha_{21} & \alpha_{22} & \alpha_{23} \\ e_{31} & e_{32} & e_{33} & e_{34} & e_{35} & e_{36} & \kappa_{31} & \kappa_{32} & \kappa_{33} & \alpha_{31} & \alpha_{32} & \alpha_{33} \\ q_{11} & q_{12} & q_{13} & q_{14} & q_{15} & q_{16} & \alpha_{11} & \alpha_{12} & \alpha_{13} & -\mu_{11} & -\mu_{12} & -\mu_{13} \\ q_{21} & q_{22} & q_{23} & q_{24} & q_{25} & q_{26} & \alpha_{21} & \alpha_{22} & \alpha_{23} & -\mu_{21} & -\mu_{22} & -\mu_{23} \\ q_{31} & q_{32} & q_{33} & q_{34} & q_{35} & q_{36} & \alpha_{31} & \alpha_{32} & \alpha_{33} & -\mu_{31} & -\mu_{32} & -\mu_{33} \end{bmatrix},\ \mathbf{\Gamma} = \begin{bmatrix} \Lambda_1 \\ \Lambda_2 \\ \Lambda_3 \\ \Lambda_4 \\ \Lambda_5 \\ \Lambda_6 \\ \rho_1 \\ \rho_2 \\ \rho_3 \\ \lambda_1 \\ \lambda_2 \\ \lambda_3 \end{bmatrix} \tag{8}$$

2.1. Nonlinear magnetostrictive constitutive equation

Considering the nonlinear strain response under the magnetic field loading, it is imperative to establish a nonlinear constitutive relationship defining the magneto-elastic coupling. The internal energy density function $U\left(\varepsilon_{ij},\ M_k,\ S\right)$, which encompasses strain components ε_{ij}, magnetization components M_i, and entropy density S, is presented as follows:

$$dU(\varepsilon_{ij}, M_k, S) = \sigma_{ij} d\varepsilon_{ij} + \mu_0 H_k dM_k + TdS \tag{9}$$

The equation of thermodynamics in the form of the Gibbs free energy function is employed as follows:

$$G\left(\sigma_{ij}, \boldsymbol{M_k}, T\right) = U - TS - \sigma_{ij}\varepsilon_{ij} \tag{10}$$

In order to determine the strain component ε_{ij} and the magnetic field intensity component H_k, the partial derivatives of the Gibbs free energy function with respect to stress and magnetization are deduced, resulting in the following thermodynamic relations:

$$\varepsilon_{ij} = \frac{\partial G\left(\sigma_{ij}, M_k, T\right)}{\partial \sigma_{ij}},\ \mu_0 H_k = \frac{\partial G\left(\sigma_{ij}, M_k, T\right)}{\partial M_k} \tag{11}$$

A second-order Taylor expansion of the Gibbs free energy function shown in Eq. (10) at a steady state $(\sigma_{ij}, M_k) = (0,0)$ is substituted into Eq. (11) to obtain polynomial equations with the stress and magnetization as variables. The coupled magneto-elastic nonlinear constitutive relation is employed to describe the above magnetostrictive nonlinear characteristics as follows:

$$\begin{aligned} \varepsilon_{ij} = {} & \frac{1}{E}\left[(1+\nu)\sigma_{ij} - \nu\sigma_{kk}\delta_{ij}\right] + \frac{\lambda_s}{\sigma_s}\left(\frac{3}{2}\sigma_{ij} - \frac{1}{2}\sigma_{kk}\delta_{ij}\right) + \\ & \frac{1}{M_s^2}\left\{\frac{3}{2}\lambda_s M_i M_j - M_k M_k\left[\frac{\lambda_s}{2}\delta_{ij} + \frac{\lambda_S\left(\frac{3}{2}\sigma_{ij} - \frac{1}{2}\sigma_{kk}\delta_{ij}\right)}{\sigma_s}\right]\right\} \end{aligned} \tag{12}$$

where E and ν mean the Young's modulus and Poisson's ratio. λ_s, M_s and σ_s represent the saturation magnetostrictive strain, saturation magnetization and maximum pre-stress, respectively. δ_{ij} is the Kronecker delta. The magnetic field intensity components H_k in Eq. (11) can be further reformulated as:

$$H_k = \frac{1}{k(T)M} L^{-1}\left(\frac{M}{M_s(T)}\right) M_k - \frac{\lambda_s}{\mu_0 M_s^2}\left[3\sigma_{ij} - \sigma_{kk}\delta_{ij} - \left(\frac{3\sigma_{ij}^2 - \sigma_{kk}^2}{2}\right)\frac{\delta_{ij}}{\sigma_s}\right] M_j, \tag{13}$$

where $L^{-1}(.)$ means the inverse of the Langevin function $L(x) = \coth(x) - 1/x$. $k(T) = \frac{3\chi_m}{M_S(T)}$ is the relaxation factor with magnetic susceptibility χ_m. $M_s(T) = M_s\left(\frac{1 - T/T_c}{1 - T_0/T}\right)^{1/2}$ is the temperature-dependent saturation magnetization. $M = \sqrt{M_1^2 + M_2^2 + M_3^2}$ denotes the modulus of the magnetization matrix.

To describe the nonlinear response of magnetic field intensity with respect to magnetostrictive

properties, the incremental form of strain and magnetic field intensity in Eqs. (12) and (13) is introduced and expressed in matrix, as follows:

$$\begin{bmatrix} \mathbf{\Delta\sigma} \\ \mathbf{\Delta B} \end{bmatrix} = \begin{bmatrix} \mathbf{C} & \mathbf{q}^{\mathrm{T}} \\ \mathbf{q} & \mathbf{-\mu} \end{bmatrix} \begin{bmatrix} \mathbf{\Delta\varepsilon} \\ \mathbf{-\Delta H} \end{bmatrix} - \begin{bmatrix} \mathbf{\Lambda} \\ \boldsymbol{\lambda} \end{bmatrix} \Delta T \tag{14}$$

where $\mathbf{\Delta\sigma} = \left[\Delta\sigma_{11} \quad \Delta\sigma_{22} \quad \Delta\sigma_{33} \quad \Delta\sigma_{23} \quad \Delta\sigma_{13} \quad \Delta\sigma_{12}\right]^T$, $\mathbf{\Delta H} = \left[\Delta H_1 \quad \Delta H_2 \quad \Delta H_3\right]^T$, $\mathbf{\Delta B} = \left[\Delta B_1 \quad \Delta B_2 \quad \Delta B_3\right]^T$, $\mathbf{\Delta\varepsilon} = \left[\Delta\varepsilon_{11} \quad \Delta\varepsilon_{22} \quad \Delta\varepsilon_{33} \quad 2\Delta\varepsilon_{23} \quad 2\Delta\varepsilon_{13} \quad 2\Delta\varepsilon_{12}\right]^T$.

To determinate the nonlinear magnetostrictive coefficient matrix $\mathbf{L} = \begin{bmatrix} \mathbf{C} & \mathbf{q}^{\mathrm{T}} \\ \mathbf{q} & \mathbf{-\mu} \end{bmatrix}$ and pyromagnetic coefficient vector $\mathbf{R} = \begin{bmatrix} \mathbf{\Lambda} \\ \boldsymbol{\lambda} \end{bmatrix}$ in Eq. (14), the combination of the partial derivatives of Eqs. (12) and (13) should be conducted as follows:

$$\left[\mathbf{C}\right]^{-1} = \frac{\partial\varepsilon}{\partial\sigma}, \ \left[\mathbf{q}\right]^{-1} = \frac{\partial \boldsymbol{H}}{\partial\sigma}, \ \left[\boldsymbol{\mu}\right]^{-1} = \frac{\partial \boldsymbol{H}}{\partial \boldsymbol{M}}, \ \left[\mathbf{\Lambda}\right]^{-1} = \frac{\partial\varepsilon}{\partial T}, \ \left[\boldsymbol{\lambda}\right]^{-1} = \frac{\partial \boldsymbol{H}}{\partial T} \tag{15}$$

To solve the Eq. (14), the boundary condition should be considered: Without consideration of external load, free charge density and magnetic flux density, the incremental constitutive equations mentioned above satisfy the stress equilibrium and Maxwell's equations in the Cartesian coordinates x_i, that is,

$$\frac{\partial\sigma_{ij}}{\partial x_j} = 0, \ \frac{\partial D_i}{\partial x_i} = 0, \ \frac{\partial B_i}{\partial x_i} = 0 \tag{16}$$

where the components of the magnetic flux density B_i are related to magnetic field density components H_i and magnetization components M_i in the form $B_i = \mu_0\left(H_i + M_i\right)$.

2.2. Linear piezoelectric constitutive equation

To investigate the mechanical properties of piezoelectric composites, a linear piezoelectric coupling constitutive relation is adopted. The mechanical stress tensor σ_{ij} and electric displacement vector D_i are commonly defined by Eqs. (17)-(18):

$$\sigma_{ij} = C_{ijkl}\varepsilon_{kl} - e_{kij}E_k \tag{15}$$

$$D_i = e_{kij}\varepsilon_{kl} + \kappa_{ik}E_k \tag{16}$$

where ε_{kl} and E_k represent the strain tensor and electric field vector, respectively. Alternatively,

Eqs. (17)-(18) can be reformulated into a matrix form as follows:

$$\begin{bmatrix} \boldsymbol{\sigma} \\ \mathbf{D} \end{bmatrix} = \begin{bmatrix} \mathbf{C} & -\mathbf{e}^{\mathrm{T}} \\ \mathbf{e} & \boldsymbol{\kappa} \end{bmatrix} \begin{bmatrix} \boldsymbol{\varepsilon} \\ \mathbf{E} \end{bmatrix} = \mathbf{P} \begin{bmatrix} \boldsymbol{\varepsilon} \\ \mathbf{E} \end{bmatrix} \tag{17}$$

where $\mathbf{C}$, $\mathbf{e}$ and $\boldsymbol{\kappa}$ are the 6×6 elastic stiffness coefficient matrix, 6×3 piezoelectric coefficient matrix, and 3×3 relative permittivity coefficient matrix, respectively. $\mathbf{P} = \begin{bmatrix} \mathbf{C} & -\mathbf{e}^{\mathrm{T}} \\ \mathbf{e} & \boldsymbol{\kappa} \end{bmatrix}$ denotes the electro-elastic property matrix.

3. Micromechanical model of FVDAM

In this section, a microscopic mechanical model of periodic structure is established to study the nonlinear mechanical-electric-magnetic coupling behavior of ME composites. Continuous fibers are used as magnetostrictive reinforcements surrounded by piezoelectric matrix. As shown in Fig. 2, the representative volume element (RVE) containing microscopic features is applied for numerical model analysis. The nonlinear magnetoelectric coupling constitutive relationship proposed in Section 2 is implemented into the finite volume direct averaging micromechanics (FVDAM) model. Using this microscopic modeling strategy, the changes in displacement, electric potential and magnetic potential are considered in the two-scale modeling of structures - macroscopic composites involving the global $x_1 - x_2 - x_3$ coordinates and microstructure referring to the local $y_2 - y_3$ coordinates, respectively.

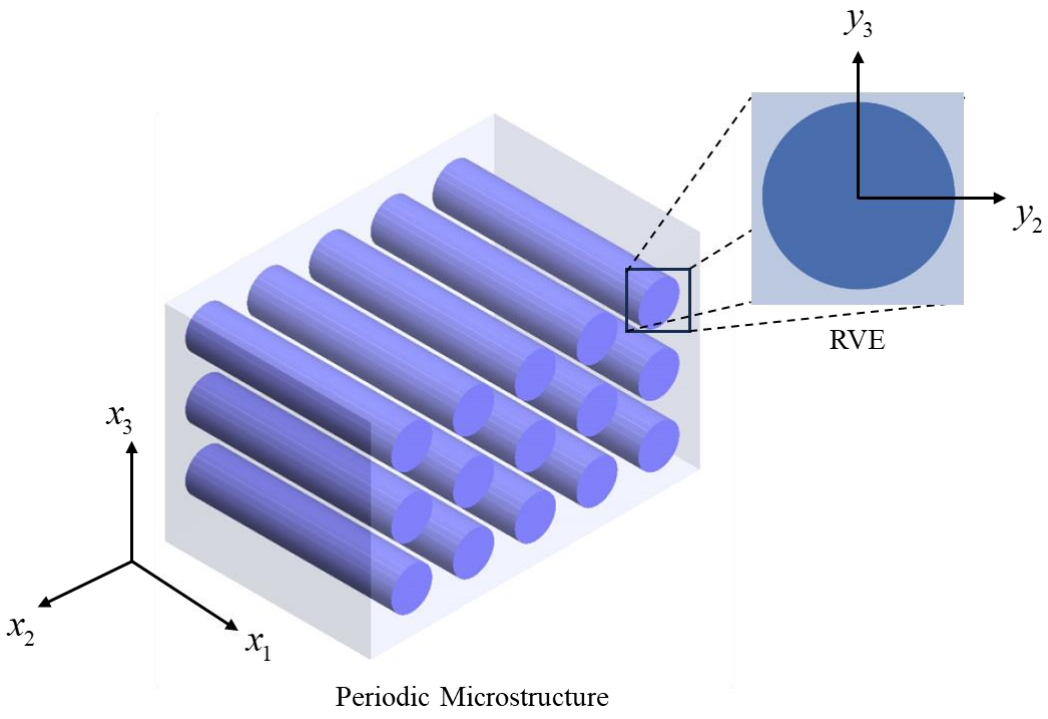

Fig. 2. Schematic diagram of the periodic microstructure.

3.1. Parametric element mapping relationship

The multi-physics analysis using the FVDAM model is based on the principle of asymptotic homogenization theory and introduces the electric potential and magnetic potential fields to effectively solve the prediction problem of the equivalent physical and mechanical properties of ME composites. The present micromechanical model considers surface average quantities instead of nodal physical quantities as the unknowns, and a parameterized convex quadrilateral mesh is proposed to discretize the representative volume elements, as shown in Fig. 3 (a). The $N_\beta \times N_\gamma$ parametric elements are used to discretize the RVE, which could be defined by a curved surface of the microscopic geometry. The subscripts β and γ are the location indexes of the element in y_2 and y_3 directions, respectively. The location of the actual microstructure is determined by the vertices $(y_2^{(m)}, y_3^{(m)})^{(\beta,\gamma)}$ of the discretized sub-cells located in the natural $y_2 - y_3$ coordinate system (y_1 denotes the axial direction). The coordinate mapping relationship is defined as:

$$y_i^{(\beta,\gamma)}(y_2, y_3) = \sum_{m=1}^{4} N_m(\eta, \xi) y_i^{(\beta,\gamma)} \quad i = 1,2,3 \tag{18}$$

where

$$\begin{aligned} N_1 &= \frac{1}{4}(1-\xi)(1-\eta) \qquad N_2 = \frac{1}{4}(1-\xi)(1+\eta) \\ N_3 &= \frac{1}{4}(1+\xi)(1+\eta) \qquad N_4 = \frac{1}{4}(1+\xi)(1-\eta) \end{aligned} \tag{19}$$

The subscripts $m = 1,2,3,4$ denotes the boundary sequence number of the quadrilateral. The shape functions $N_m(\eta, \xi)$ are used to characterize the mapping relation between the coordinate system and the reference coordinate system. Using the Q4-type parameter mapping function $N_m(\eta, \xi)$, the regular quadrilateral sub-cell in the reference $\eta - \xi$ coordinates system is mapped to a quadrilateral sub-cell in the actual microstructure shown in Figs. 3(b) and (c), thus the $(\beta, \gamma)^{th}$ parametric element is generated.

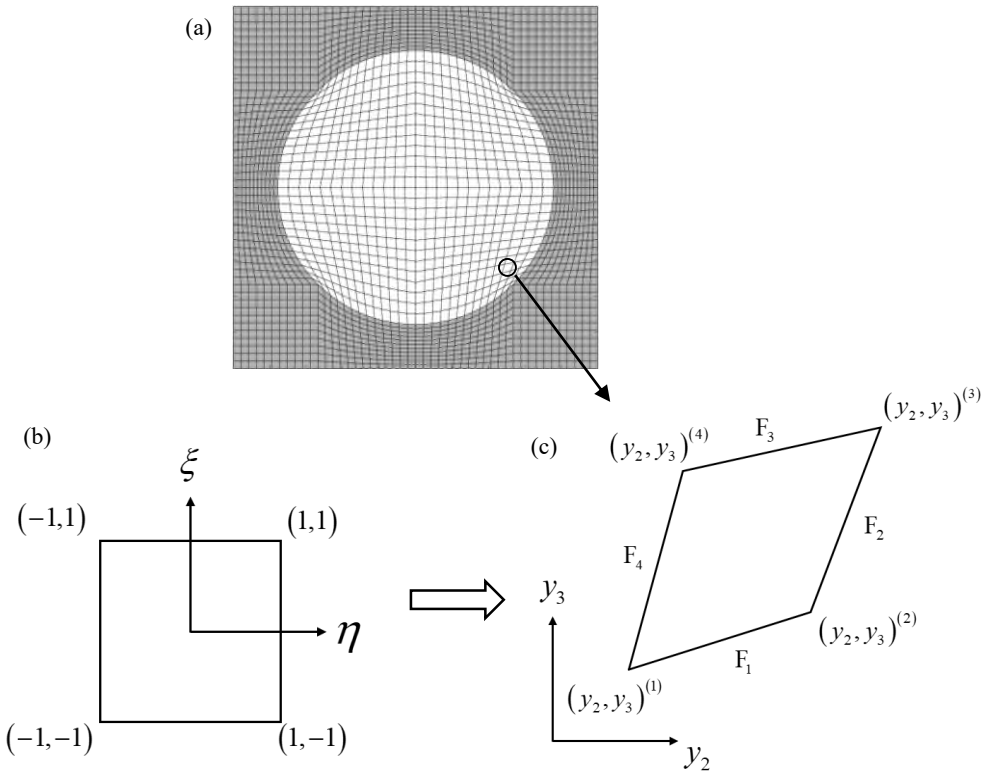

Fig. 3. Mapping of the reference sub-cell in the $\eta-\xi$ coordinates system onto a quadrilateral sub-cell in the y_2-y_3 coordinate system. (a) Parameterized discrete elements, (b) Reference coordinate system and (c) Natural coordinate system.

As the fundamental assumption in zero-order homogenization theory [41] is stated, the microstructure scale is infinitesimal with respect to the macroscopic structure size in the FVDAM model. As a result, the local stresses, electric displacements, and magnetic flux density at the microstructural scale include the macroscopic average contributions and the microscopic fluctuating contributions located on the global $x_1-x_2-x_3$ coordinates and the y_2-y_3 local coordinates, respectively. Thus, the displacement components, electric potential components and magnetic potential components are represented in incremental form as follows:

$$\Delta u_i^{(\beta,\gamma)} = \Delta\bar{\varepsilon}_{ij}x_j + \Delta u_i'^{(\beta,\gamma)} \tag{20}$$

$$\Delta f^{(\beta,\gamma)} = -\Delta\bar{E}_j x_j + \Delta f'^{(\beta,\gamma)} \tag{21}$$

$$\Delta\phi^{(\beta,\gamma)} = -\Delta\bar{H}_j x_j + \Delta\phi'^{(\beta,\gamma)} \tag{22}$$

The quantities $\Delta u_i'^{(\alpha,\beta)}$, $\Delta f'^{(\alpha,\beta)}$ and $\Delta\phi'^{(\beta,\gamma)}$ are the sub-cell fluctuating displacement, electric potential components and magnetic potential components located in the local y_2-y_3 coordinate system. The local strain, electric field intensity and magnetic field intensity in the sub-cells are determined by the macroscopic quantity and fluctuation components defined in Eqs. (25)-(27),

$$\Delta\varepsilon_{ij}^{(\beta,\gamma)} = \Delta\bar{\varepsilon}_{ij} + \Delta\varepsilon_{ij}'^{(\beta,\gamma)} = \Delta\bar{\varepsilon}_{ij} + \frac{1}{2}\Delta\left(\frac{\partial u_i'}{\partial y_j} + \frac{\partial u_j'}{\partial y_i}\right)^{(\beta,\gamma)} \tag{23}$$

$$\Delta E_j^{(\beta,\gamma)} = \Delta\bar{E}_j + \Delta E_j'^{(\beta,\gamma)} = \Delta\bar{E}_j - \Delta\left(\frac{\partial f'}{\partial y_j}\right)^{(\beta,\gamma)} \tag{24}$$

$$\Delta H_j^{(\beta,\gamma)} = \Delta\bar{H}_j + \Delta H_j'^{(\beta,\gamma)} = \Delta\bar{H}_{jj} - \Delta\left(\frac{\partial \phi'}{\partial y_j}\right)^{(\beta,\gamma)} \tag{25}$$

where $\Delta\bar{\varepsilon}_{ij}$, $\Delta\bar{E}_j$ and $\Delta\bar{H}_j$ are the increment of macroscopic strain, electric field intensity and magnetic field intensity components, respectively. Especially, $\Delta\varepsilon_{11}^{(\beta,\gamma)} = \Delta\bar{\varepsilon}_{11}$, $\Delta E_1^{(\beta,\gamma)} = \Delta\bar{E}_1$ and $\Delta H_1^{(\beta,\gamma)} = \Delta\bar{H}_1$ are observed due to the continuous fiber reinforcement in the axial y_1 - direction. The partial differential $\partial/\partial y_j$ regarding the fluctuation components defined in Eqs. (25)-(27) is transformed into $\frac{\partial}{\partial y} \to \frac{\partial}{\partial \eta}$ by the Jacobian matrix **J** in the coordinate transformation process, that is,

$$\begin{bmatrix} \frac{\partial u_i'}{\partial y_2} \\ \frac{\partial u_i'}{\partial y_3} \end{bmatrix}^{(\beta,\gamma)} = \mathbf{J}^{-1}\begin{bmatrix} \frac{\partial u_i'}{\partial \eta} \\ \frac{\partial u_i'}{\partial \xi} \end{bmatrix}^{(\beta,\gamma)}, \begin{bmatrix} \frac{\partial f'}{\partial y_2} \\ \frac{\partial f'}{\partial y_3} \end{bmatrix}^{(\beta,\gamma)} = \mathbf{J}^{-1}\begin{bmatrix} \frac{\partial f'}{\partial \eta} \\ \frac{\partial f'}{\partial \xi} \end{bmatrix}^{(\beta,\gamma)}, \begin{bmatrix} \frac{\partial \phi'}{\partial y_2} \\ \frac{\partial \phi'}{\partial y_3} \end{bmatrix}^{(\beta,\gamma)} = \mathbf{J}^{-1}\begin{bmatrix} \frac{\partial \phi'}{\partial \eta} \\ \frac{\partial \phi'}{\partial \xi} \end{bmatrix}^{(\beta,\gamma)} \tag{26}$$

where

$$\mathbf{J} = \begin{bmatrix} \sum_{m=1}^{4}\frac{\partial N_m}{\partial \eta} y_2^{(m)} & \sum_{m=1}^{4}\frac{\partial N_m}{\partial \xi} y_3^{(m)} \\ \sum_{m=1}^{4}\frac{\partial N_m}{\partial \eta} y_2^{(m)} & \sum_{m=1}^{4}\frac{\partial N_m}{\partial \xi} y_3^{(m)} \end{bmatrix}, \ \mathbf{J}^{-1} = \begin{bmatrix} \hat{J}_{22} & \hat{J}_{23} \\ \hat{J}_{32} & \hat{J}_{33} \end{bmatrix} \tag{27}$$

3.2. Generalization of the local stiffness matrix

The sub-cell fluctuating displacement $\Delta u_i'^{(\beta,\gamma)}$, electric potential components $\Delta f'^{(\beta,\gamma)}$ and magnetic potential components $\Delta\phi'^{(\beta,\gamma)}$ are expanded into the second-order polynomials in the reference $\eta-\xi$ coordinate system according to the asymptotic homogenization theory [42], that is,

$$\Delta u_i'^{(\beta,\gamma)} = \Delta W_{i(00)}^{(\beta,\gamma)} + \eta\Delta W_{i(10)}^{(\beta,\gamma)} + \xi\Delta W_{i(01)}^{(\beta,\gamma)} + \frac{1}{2}\left(3\eta^2-1\right)\Delta W_{i(20)}^{(\beta,\gamma)} + \frac{1}{2}\left(3\xi^2-1\right)\Delta W_{i(02)}^{(\beta,\gamma)} \tag{28}$$

$$\Delta f'^{(\beta,\gamma)} = \Delta W_{4(00)}^{(\beta,\gamma)} + \eta\Delta W_{4(10)}^{(\beta,\gamma)} + \xi\Delta W_{4(01)}^{(\beta,\gamma)} + \frac{1}{2}\left(3\eta^2-1\right)\Delta W_{4(20)}^{(\beta,\gamma)} + \frac{1}{2}\left(3\xi^2-1\right)\Delta W_{4(02)}^{(\beta,\gamma)} \tag{29}$$

$$\Delta\phi'^{(\beta,\gamma)} = \Delta W_{5(00)}^{(\beta,\gamma)} + \eta\Delta W_{5(10)}^{(\beta,\gamma)} + \xi\Delta W_{5(01)}^{(\beta,\gamma)} + \frac{1}{2}\left(3\eta^2-1\right)\Delta W_{5(20)}^{(\beta,\gamma)} + \frac{1}{2}\left(3\xi^2-1\right)\Delta W_{5(02)}^{(\beta,\gamma)} \tag{30}$$

where the intermediate variables $\Delta W_{(10)}^{(\beta,\gamma)}$ and $\Delta W_{(01)}^{(\beta,\gamma)}$ represent the first-order fluctuating contributions in the η and ξ directions, respectively. Similarly, $\Delta W_{(20)}^{(\beta,\gamma)}$ and $\Delta W_{(02)}^{(\beta,\gamma)}$ denote the second-order fluctuating contributions. Combining the above polynomial expansions, the sub-cell surface integral equation are as follows:

$$\Delta\hat{u}_i'^{(1),(3)} = \frac{1}{2}\int_{-1}^{+1} \Delta u_i'(\eta, \mp 1)\, d\eta \qquad \Delta\hat{u}_i'^{(2),(4)} = \frac{1}{2}\int_{-1}^{+1} \Delta u_i'(\pm 1, \xi)\, d\xi \tag{31}$$

$$\Delta\hat{f}'^{(1),(3)} = \frac{1}{2}\int_{-1}^{+1} \Delta f'(\eta, \mp 1)\, d\eta \qquad \Delta\hat{f}'^{(2),(4)} = \frac{1}{2}\int_{-1}^{+1} \Delta f'(\pm 1, \xi)\, d\xi \tag{32}$$

$$\Delta\hat{\phi}'^{(1),(3)} = \frac{1}{2}\int_{-1}^{+1} \Delta \phi'(\eta, \mp 1)\, d\eta \qquad \Delta\hat{\phi}'^{(2),(4)} = \frac{1}{2}\int_{-1}^{+1} \Delta \phi'(\pm 1, \xi)\, d\xi \tag{33}$$

where the superscripts (1), (2), (3) and (4) represent the vortex number of the sub-cell shown in Fig. 3(c). Substituting the second-order polynomials in Eqs. (30)-(32), the fluctuating surface-averaged displacements $\Delta\hat{u}_i'$, electric potentials $\Delta\hat{f}'$ and magnetic potentials $\Delta\hat{\phi}'$ on faces F_1, F_3 ($\eta = \pm 1$) and F_2, F_4 ($\xi = \mp 1$) can be evaluated by the integral governing Eqs (33)-(35), that is,

$$\Delta\hat{u}_i'^{(1),(3)} = \Delta W_{i(00)} \mp \Delta W_{i(01)} + \Delta W_{i(00)} \qquad \Delta\hat{u}_i'^{(2),(4)} = \Delta W_{i(00)} \pm \Delta W_{i(01)} + \Delta W_{i(00)} \tag{34}$$

$$\Delta\hat{f}'^{(1),(3)} = \Delta W_{4(00)} \mp \Delta W_{4(01)} + \Delta W_{4(00)} \qquad \Delta\hat{f}'^{(2),(4)} = \Delta W_{4(00)} \pm \Delta W_{4(01)} + \Delta W_{4(00)} \tag{35}$$

$$\Delta\hat{\phi}'^{(1),(3)} = \Delta W_{5(00)} \mp \Delta W_{5(01)} + \Delta W_{5(00)} \qquad \Delta\hat{\phi}'^{(2),(4)} = \Delta W_{5(00)} \pm \Delta W_{5(01)} + \Delta W_{5(00)} \tag{36}$$

For the crossover operation of Eqs. (36)-(38), the four intermediate variables $\Delta W_{(01)}^{(\beta,\gamma)}$, $\Delta W_{(10)}^{(\beta,\gamma)}$, $\Delta W_{(02)}^{(\beta,\gamma)}$ and $\Delta W_{(20)}^{(\beta,\gamma)}$ are expressed as functions of the surface-averaged components and zero-order intermediate variable $\Delta W_{(00)}^{(\beta,\gamma)}$, that is,

$$\begin{bmatrix} \Delta W_{i(10)} \\ \Delta W_{i(01)} \\ \Delta W_{i(20)} \\ \Delta W_{i(02)} \end{bmatrix} = \frac{1}{2}\begin{bmatrix} 0 & 1 & 0 & -1 \\ -1 & 0 & 1 & 0 \\ 0 & 1 & 0 & 1 \\ 1 & 0 & 1 & 0 \end{bmatrix}\begin{bmatrix} \Delta\hat{u}_i'^{(1)} - \Delta W_{i(00)} \\ \Delta\hat{u}_i'^{(2)} - \Delta W_{i(00)} \\ \Delta\hat{u}_i'^{(3)} - \Delta W_{i(00)} \\ \Delta\hat{u}_i'^{(4)} - \Delta W_{i(00)} \end{bmatrix} \tag{37}$$

Similar to Eqs (33)-(35), the increments of the surface-averaged traction $\Delta\hat{t}_i$, normal electric displacements $\Delta\hat{D}_n$ and normal magnetic flux density $\Delta\hat{B}_n$ are derived by integrating the corresponding interfacial components on faces F_1, F_3 ($\eta = \pm 1$) and F_2, F_4 ($\xi = \mp 1$), that is,

$$\Delta\hat{t}_i^{(1,3)} = \frac{1}{2}\int_{-1}^{+1} \Delta t_i\left(\eta, \mp 1\right) d\eta \qquad \Delta\hat{t}_i^{(2,4)} = \frac{1}{2}\int_{-1}^{+1} \Delta t_i\left(\pm 1, \xi\right) d\xi \tag{38}$$

$$\Delta\hat{D}_n^{(1,3)} = \frac{1}{2}\int_{-1}^{+1} \Delta D_n\left(\eta, \mp 1\right) d\eta \qquad \Delta\hat{D}_n^{(2,4)} = \frac{1}{2}\int_{-1}^{+1} \Delta D_n\left(\pm 1, \xi\right) d\xi \tag{39}$$

$$\Delta\hat{B}_n^{(1,3)} = \frac{1}{2}\int_{-1}^{+1} \Delta B_n\left(\eta, \mp 1\right) d\eta \qquad \Delta\hat{B}_n^{(2,4)} = \frac{1}{2}\int_{-1}^{+1} \Delta B_n\left(\pm 1, \xi\right) d\xi \tag{40}$$

where the unit normal vector n_i denotes the vertical direction vector of the quadrilateral element surface on face F_m. The surface traction Δt_i, normal electric displacement ΔD_n and normal magnetic flux density ΔB_n are defined by:

$$\Delta t_1 = \left[n_2\Delta\sigma_{12} + n_3\Delta\sigma_{13}\right] \tag{41}$$

$$\Delta t_2 = \left[n_2\Delta\sigma_{22} + n_3\Delta\sigma_{23}\right] \tag{42}$$

$$\Delta t_3 = \left[n_2\Delta\sigma_{23} + n_3\Delta\sigma_{33}\right] \tag{43}$$

$$\Delta D_n = \left[n_2\Delta D_2 + n_3\Delta D_3\right] \tag{44}$$

$$\Delta B_n = \left[n_2\Delta B_2 + n_3\Delta B_3\right] \tag{45}$$

Substituting the electro-magneto-thermo-elastic coupling constitutive relation in Eqs. (4) into Eqs. (43)-(47), the relationship between the macroscopic load and the local response of the sub-cell can be further formulated into a matrix form:

$$\mathbf{I}^{(m)} = \mathbf{N}^{(m)}\mathbf{G}\boldsymbol{\Delta}\bar{\mathbf{X}} - \mathbf{N}^{(m)}\boldsymbol{\Gamma}\Delta T \tag{46}$$

where

$$\mathbf{N}^{(m)} = \begin{bmatrix} 0 & 0 & 0 & 0 & n_3 & n_2 & 0 & 0 & 0 & 0 & 0 & 0 \\ 0 & n_2 & 0 & n_3 & 0 & 0 & 0 & 0 & 0 & 0 & 0 & 0 \\ 0 & 0 & n_3 & n_2 & 0 & 0 & 0 & 0 & 0 & 0 & 0 & 0 \\ 0 & 0 & 0 & 0 & 0 & 0 & 0 & n_2 & n_3 & 0 & 0 & 0 \\ 0 & 0 & 0 & 0 & 0 & 0 & 0 & 0 & 0 & 0 & n_2 & n_3 \end{bmatrix}^{(m)} \tag{47}$$

$$\mathbf{I}^{(m)} = \left[\Delta\hat{t}_1^{(m)} \quad \Delta\hat{t}_2^{(m)} \quad \Delta\hat{t}_3^{(m)} \quad \Delta\hat{D}_n^{(m)} \quad \Delta\hat{B}_n^{(m)}\right]^T \tag{48}$$

The orientation matrix $\mathbf{N}^{(m)}$ contains the normal vector of the sub-cell boundary. $\mathbf{I}^{(m)}$ denotes the vector determinants of the surface-averaged traction, normal electric displacement, and normal flux density. The macroscopic load vector $\boldsymbol{\Delta}\mathbf{X}$ is defined by constitutive relation in Eq. (5). Taking into account the stress equilibrium and Maxwell's equations in Eq. (15), the surface-averaged traction,

normal electric displacements and normal magnetic flux density on each side of F_m are obtained by the integration,

$$\int_l \Delta\hat{t}_i^{(m)} dl = \sum_{m=1}^{4} l_m \Delta t_i = 0 \tag{49}$$

$$\int_l \Delta\hat{D}_n^{(m)} dl = \sum_{m=1}^{4} l_m \Delta D_n = 0 \tag{50}$$

$$\int_l \Delta\hat{B}_n^{(m)} dl = \sum_{m=1}^{4} l_m \Delta B_n = 0 \tag{51}$$

Combining the coordinate transformation process in Eqs. (25)-(28) and the second-order polynomial of the fluctuating components in Eqs. (30)-(32), a complete form of the local equilibrium equations (see Appendix) is achieved. The first- and second-order intermediate variables $\Delta W_{(01)}^{(\beta,\gamma)}$, $\Delta W_{(10)}^{(\beta,\gamma)}$, $\Delta W_{(02)}^{(\beta,\gamma)}$ and $\Delta W_{(20)}^{(\beta,\gamma)}$ are eliminated according to the surface integral Eq. (39), and the zero-order intermediate variable $\Delta W_{(00)}^{(\alpha,\beta)}$ is expressed in the matrix form as a function of the surface-averaged displacement, potential, and magnetic potential, as follows:

$$\begin{bmatrix} W_{1(00)} \\ W_{2(00)} \\ W_{3(00)} \\ W_{4(00)} \\ W_{5(00)} \end{bmatrix} = \mathbf{L}^{-1}\mathbf{R} \begin{bmatrix} \Delta\hat{u}_1'^{(1)} + \Delta\hat{u}_1'^{(2)} \\ \Delta\hat{u}_1'^{(3)} + \Delta\hat{u}_1'^{(4)} \\ \Delta\hat{u}_2'^{(1)} + \Delta\hat{u}_2'^{(2)} \\ \Delta\hat{u}_2'^{(3)} + \Delta\hat{u}_2'^{(4)} \\ \Delta\hat{u}_3'^{(1)} + \Delta\hat{u}_3'^{(2)} \\ \Delta\hat{u}_3'^{(3)} + \Delta\hat{u}_3'^{(4)} \\ \Delta\hat{f}'^{(1)} + \Delta\hat{f}'^{(2)} \\ \Delta\hat{f}'^{(3)} + \Delta\hat{f}'^{(4)} \\ \Delta\hat{\phi}'^{(1)} + \Delta\hat{\phi}'^{(2)} \\ \Delta\hat{\phi}'^{(3)} + \Delta\hat{\phi}'^{(4)} \end{bmatrix} \tag{52}$$

where the elements in the matrices $\mathbf{L}$ and $\mathbf{R}$ in Eq. (54) are given explicitly in Appendix. The surface-averaged tractions $\Delta\hat{t}_i$, normal electric displacements $\Delta\hat{D}_n$ and normal magnetic flux density $\Delta\hat{B}_n$ in Eqs. (51)-(53) can be further written as an ensemble matrix $\mathbf{U}^{(\beta,\gamma)}$ containing the surface-averaged displacements, electric potential, and magnetic potential by assembling the local stiffness matrix in sub-cell. The final relations of the $(\beta,\gamma)^{th}$ sub-cell on each face can be written in a matrix form as follows,

$$\begin{bmatrix}\mathbf{I}^{(1)}\\ \mathbf{I}^{(2)}\\ \mathbf{I}^{(3)}\\ \mathbf{I}^{(4)}\end{bmatrix}^{(\beta,\gamma)}=\begin{bmatrix}\mathbf{N}^{(1)}\\ \mathbf{N}^{(2)}\\ \mathbf{N}^{(3)}\\ \mathbf{N}^{(4)}\end{bmatrix}^{(\beta,\gamma)}\mathbf{G}^{(\beta,\gamma)}\Delta\mathbf{X}+\mathbf{K}_{local}^{(\beta,\gamma)}\mathbf{U}^{(\beta,\gamma)}+\begin{bmatrix}\mathbf{N}^{(1)}\\ \mathbf{N}^{(2)}\\ \mathbf{N}^{(3)}\\ \mathbf{N}^{(4)}\end{bmatrix}^{(\beta,\gamma)}\mathbf{\Gamma}^{(\beta,\gamma)}\Delta T \tag{53}$$

where

$$\Delta\mathbf{X}=\left[\Delta\bar{\varepsilon}_{11},\Delta\bar{\varepsilon}_{22},\Delta\bar{\varepsilon}_{33},2\Delta\bar{\varepsilon}_{23},\ 2\Delta\bar{\varepsilon}_{13},2\Delta\bar{\varepsilon}_{12},-\Delta\bar{E}_1,-\Delta\bar{E}_2,-\Delta\bar{E}_3,-\Delta\bar{H}_1,-\Delta\bar{H}_2,-\Delta\bar{H}_3\right]$$

$$\mathbf{U}^{(\beta,\gamma)}=\left[\mathbf{u}^{(1)},\ \mathbf{u}^{(2)},\ \mathbf{u}^{(3)},\ \mathbf{u}^{(4)}\right]^{(\beta,\gamma)}\ \text{with}\ \mathbf{u}^{(m)}=\left[\Delta\hat{u}_1',\ \Delta\hat{u}_2',\ \Delta\hat{u}_3',\ \Delta\hat{f}',\ \Delta\hat{\phi}'\right]^{(m)}$$

Finally, the generalized local stiffness matrices $\mathbf{K}_{local}^{(\beta,\gamma)}$ including 20×20 elements are obtained by the sub-cell geometry and material properties.

3.3. Assembly of global stiffness matrix

According to the parametric FVDAM theory, the internal continuity and integrity of the material are assumed after deformation, ensuring that the surface traction force, normal electric displacement, and normal magnetic flux density on the common interface between adjacent sub-cells satisfy the continuous conditions. Moreover, the above physical parameters follow periodic boundary conditions at the RVE boundary. To assemble the global stiffness matrix, the following continuous and periodic conditions of surface traction matrices $\mathbf{I}^{(\beta,\gamma)}$ and displacement matrices $\mathbf{u}^{(\beta,\gamma)}$ between adjacent sub-cells are imposed as follows:

(1) continuous conditions

$$\mathbf{u}^{(1)(\beta,\gamma)}=\mathbf{u}^{(3)(\beta,\gamma+1)}=\mathbf{u}^{3(\beta,\gamma+1)} \tag{54}$$

$$\mathbf{u}^{(2)(\beta+1,\gamma)}=\mathbf{u}^{(4)(\beta,\gamma)}=\mathbf{u}^{2(\beta+1,\gamma)} \tag{55}$$

$$\mathbf{I}^{(1)(\beta+1,\gamma)}+\mathbf{I}^{(3)(\beta,\gamma)}=0 \tag{56}$$

$$\mathbf{I}^{(2)(\beta+1,\gamma)}+\mathbf{I}^{(4)(\beta,\gamma)}=0 \tag{57}$$

(2) periodic conditions

$$\mathbf{u}^{(1)(\beta,1)}=\mathbf{u}^{(3)(\beta,N_\gamma)}=\mathbf{u}^{3(\beta,N_\gamma)} \tag{58}$$

$$\mathbf{u}^{(2)(1,\gamma)}=\mathbf{u}^{(4)(N_\beta,\gamma)}=\mathbf{u}^{2(N_\beta,\gamma)} \tag{59}$$

$$\mathbf{I}_i^{(3)(\beta,1)}+\mathbf{I}_i^{(3)(\beta,N_\gamma+1)}=0 \tag{60}$$

$$\mathbf{I}_i^{2(1,\gamma)}+\mathbf{I}_i^{4(N_\beta+1,\gamma)}=0 \tag{61}$$

The above conditions assemble all the sub-cells of the entire RVE into a unified entity, thereby enabling the derivation of the matrix representation for the global relation shown in Eq. (64)

$$\mathbf{K}_{\mathbf{global}}\hat{\mathbf{U}}' = \mathbf{\Delta Z}\Delta\bar{\mathbf{X}} + \Delta\mathbf{\Gamma}\Delta T \tag{62}$$

where $\mathbf{K}_{\mathbf{global}}$ represents the global stiffness matrix containing 10×10 sub-matrices. $\hat{\mathbf{U}}'$ is composed of submatrices $\mathbf{u}^{2(\beta,\gamma)}$ and $\mathbf{u}^{3(\beta,\gamma)}$ including the surface-averaged displacements $\Delta\hat{u}_1'$, electric potential $\Delta\hat{f}'$, and magnetic potential $\Delta\hat{\phi}'$ in the $(\beta,\gamma)^{th}$ sub-cell. The superscripts 2 and 3 represent the transverse y_2 - direction and longitudinal y_3 - direction of surface-averaged components, respectively. $\mathbf{\Delta Z}$ and $\Delta\mathbf{\Gamma}$ are the matrices formed by the changes in the material coefficient matrix and thermal coefficient matrix of adjacent sub-cells.

3.4. Homogenization

By solving the global stiffness matrix, the global vector $\hat{\mathbf{U}}'$ consisting of sub-cell displacement, electric potential and magnetic potential can be obtained. The application of macroscopic load $\bar{\mathbf{X}}$ on the sub-cell located at coordinate (β,γ) helps to obtain the generalized Hill electro-magnetic-elastic concentration matrices $\mathbf{A}^{(\beta,\gamma)}$.

$$\mathbf{\Delta}\bar{\mathbf{X}}^{(\beta,\gamma)} = \mathbf{A}^{(\beta,\gamma)}\bar{\mathbf{X}} \tag{63}$$

where the elements of the concentration matrix $\mathbf{A}^{(\beta,\gamma)}$ are determined by applying macroscopic strain $\Delta\bar{\varepsilon}_{ij}^{(\beta,\gamma)}$, electric field $\Delta\bar{E}_i^{(\beta,\gamma)}$ and magnetic field $\Delta\bar{H}_i^{(\beta,\gamma)}$ of the sub-cell. Subsequently, the averaged macroscopic stresses, electric displacement and magnetic flux density represented by the volume weighted sum of the local components of the sub-cells is obtained by:

$$\mathbf{\Delta}\hat{\boldsymbol{\sigma}} = \frac{1}{V}\int\mathbf{\Delta}\boldsymbol{\sigma}dV = \frac{1}{V}\sum_{\gamma=1}^{N_\gamma}\sum_{\beta=1}^{N_\beta}\int_{V_{(\beta,\gamma)}}\Delta\boldsymbol{\sigma}^{(\beta,\gamma)}dV^{(\beta,\gamma)} = \sum_{\gamma=1}^{N_\gamma}\sum_{\beta=1}^{N_\beta}V_f^{(\beta,\gamma)}\mathbf{\Delta}\boldsymbol{\sigma}^{(\beta,\gamma)} \tag{64}$$

$$\mathbf{\Delta}\hat{\mathbf{E}} = \frac{1}{V}\int\mathbf{\Delta E}dV = \frac{1}{V}\sum_{\gamma=1}^{N_\gamma}\sum_{\beta=1}^{N_\beta}\int_{V_{(\beta,\gamma)}}\Delta\boldsymbol{\sigma}^{(\beta,\gamma)}dV^{(\beta,\gamma)} = \sum_{\gamma=1}^{N_\gamma}\sum_{\beta=1}^{N_\beta}V_f^{(\beta,\gamma)}\mathbf{\Delta}\boldsymbol{\sigma}^{(\beta,\gamma)} \tag{65}$$

$$\mathbf{\Delta}\hat{\mathbf{B}} = \frac{1}{V}\int\mathbf{\Delta B}dV = \frac{1}{V}\sum_{\gamma=1}^{N_\gamma}\sum_{\beta=1}^{N_\beta}\int_{V_{(\beta,\gamma)}}\mathbf{\Delta B}^{(\beta,\gamma)}dV^{(\beta,\gamma)} = \sum_{\gamma=1}^{N_\gamma}\sum_{\beta=1}^{N_\beta}V_f^{(\beta,\gamma)}\mathbf{\Delta B}^{(\beta,\gamma)} \tag{66}$$

where $V_{(\beta,\gamma)}$ and $V_f^{(\beta,\gamma)}$ is the volume and volume fraction of the $(\beta,\gamma)^{th}$ sub-cell, respectively.

Substituting Eqs. (65)-(68) into the nonlinear magnetostrictive constitutive relation and linear piezoelectric relation defined by Eqs. (14) and (19), the macroscopic nonlinear incremental constitutive relation in each sub-cell for the electro-magneto-elastic composites is achieved as follows:

$$\mathbf{\Delta Y} = \mathbf{G}^*\mathbf{\Delta X} - \mathbf{\Gamma}^*\Delta T \tag{67}$$

where the equivalent electro-magneto-elastic coefficients matrix $\mathbf{G}^* = \begin{bmatrix} \mathbf{C}^* & \mathbf{e}^{*\mathrm{T}} & \mathbf{q}^{*\mathrm{T}} \\ \mathbf{e}^* & -\boldsymbol{\kappa}^* & -\boldsymbol{\alpha}^* \\ \mathbf{q}^* & -\boldsymbol{\alpha}^* & -\boldsymbol{\mu}^* \end{bmatrix}$ is determined by the sub-cell geometry, constitutive law and electro-magneto-elastic concentration matrix in Eq. (65). The equivalent thermal coefficients matrix $\boldsymbol{\Gamma}^* = \begin{bmatrix} \boldsymbol{\Lambda}^* \\ \boldsymbol{\rho}^* \\ \boldsymbol{\lambda}^* \end{bmatrix}$ is determined by the thermal coefficient $\boldsymbol{\Gamma}^{(\beta,\gamma)}$. The calculations of $\mathbf{G}^*$ and $\boldsymbol{\Gamma}^*$ are given as follows:

$$\mathbf{G}^* = \frac{1}{V}\sum_{\gamma=1}^{N_\gamma}\sum_{\beta=1}^{N_\beta} L_\beta L_\gamma \mathbf{G}^{(\beta,\gamma)}\mathbf{A}^{(\beta,\gamma)} \tag{68}$$

$$\boldsymbol{\Gamma}^* = \frac{1}{V}\sum_{\gamma=1}^{N_\gamma}\sum_{\beta=1}^{N_\beta} L_\beta L_\gamma \boldsymbol{\Gamma}^{(\beta,\gamma)} \tag{69}$$

4. Results and discussions

In this Section, the nonlinear modeling of coupled magnetic, mechanical, electrical properties and effects of the ME composites has been developed. In order to better understand the proposed modelling framework, Fig. 4 shows the flowchart of the nonlinear modeling process under the consideration of electro-magneto-thermo-elastic coupling behaviors. Material properties of ME composites [43–45] including piezoelectric polymers and magnetostrictive materials are provided in Table 1. The rationality of the established nonlinear model is demonstrated by two aspects. Firstly, the correctness of the developed model is verified by comparison with the experimental results. The second aspect is to enable the local distribution analysis of micromechanical model discretized with different meshes. As depicted in Fig. 4, the factors affecting the equivalent mechanical properties and nonlinear mechanical responses of ME composites are influenced by the external multi-physical field environment and the internal microstructure, respectively. Finally, the effects of these factors on ME composites are discussed.

Table1. Material properties of constituents

Material properties	Implication	Nickel	PVDF
E / GPa	Elasticity modulus	207	2.2
v	Poisson ratio	0.3	0.29
$\bar{\alpha}$ / K^{-1}	Coefficient of thermal expansion	13×10^{-6}	50×10^{-6}
$\bar{\beta}$ / K^{-1}	Coefficient of saturation magnetization thermal expansion	2.05×10^{-8}	–
λ_s	The saturation magnetostriction	4.65×10^{-5}	–
M_s / kA/m	The saturation magnetization	460	–

σ_s / MPa	Maximum pre-stress	116	–
χ_m	The magnetic susceptibility	52.152	–
e_{11} / C · m^{-2}	Piezoelectric coefficients	–	–0.1099
κ_{22} / C · V^{-1} · m^{-1}	Dielectric coefficients	–	6.64×10^{-11}

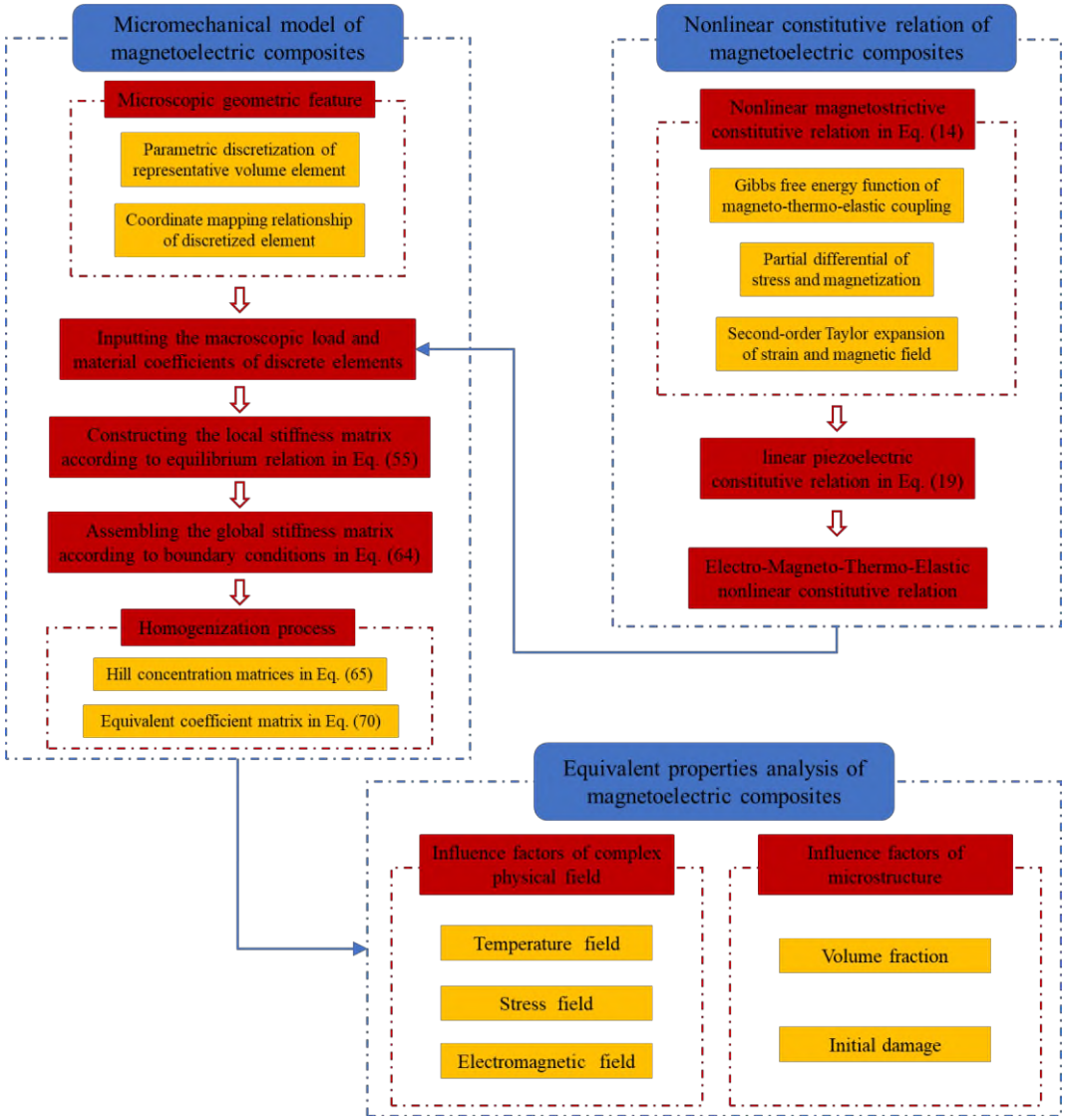

Fig. 4. The nonlinear modeling flow chart of the ME composites under electro-magneto-thermo-elastic coupling condition.

4.1. Experimental validation on FVDAM model

The experimental tests on the performance of ME composites were conducted at room temperature in Ref. [45], in which the magnetostrictive strains and coupling coefficients of the ME composites with the magnetostrictive phase composition of Nickel were obtained against the

magnetic field intensity in tests under different prestress. As compared to these experimental results, the strain response $\bar{\varepsilon}_{11}$ and the equivalent coefficient α_{ME} of the ME composites simulated using the FVDAM model under the same loading conditions are shown in Fig. 5. A volume fraction 0.25 of magnetostrictive phase is selected in this study. The numerical results obtained by the FVDAM model agree well with the experimental data at the stage of magnetic saturation. A slight deviation is observed at the initial stage of the magnetization process. As shown in Fig. 5(a), the strain under a 60 MPa prestress condition is significantly higher as compared to the strains under 20 MPa and 0 MPa conditions, demonstrating the substantial impact of prestress on magnetostriction strain. Fig. 5(b) illustrates that the ME coupling coefficient increases rapidly at low magnetic field intensities and achieves its maximum value at the magnetization saturation point, and then declines as the magnetic field intensity increases. When the magnetic field intensity $H_1 = 100$ Oe, The maximum ME coupling coefficient $\alpha_{ME}^{\max}$ reaches approximately 234 MV · cm^{-1} · Oe^{-1} under 0 MPa prestress. Under the conditions of prestresses with 20 MPa and 60 MPa, the peak values of the ME coupling coefficient decrease to approximately 175 MV · cm^{-1} · Oe^{-1} and 117 MV · cm^{-1} · Oe^{-1}, respectively. This trend indicates a reduction in the peak values of the ME coupling coefficient with the increase of prestress. As the ME coupling coefficient represents the combined response of the magnetostrictive and piezoelectric phases, the correctness of the FVDAM model could be interpreted from a theoretical point of view as follows:

$$\alpha_{ME} = \left| \frac{\Delta V_{ME}}{t \cdot \Delta H} \right| \tag{70}$$

where the ME voltage V_{ME} is derived from the piezoelectric response of the piezoelectric material induced by the magnetostrictive strain. According to the multi-physics constitutive relation in Eq. (1), the electric field intensity E_{ME} depends on the equivalent piezoelectric coefficient and the stress components. As the equivalent piezoelectric coefficient remains unaffected by the magnetic field intensity, the ME coupling coefficient α_{ME} is primarily related to the ratio of the strain increment to the magnetic field intensity increment ($\alpha_{ME} \propto \Delta\varepsilon/\Delta H$). when the magnetostrictive strain approaches stable (for example, the strain change rate $\Delta\varepsilon/\Delta H$ is approximately 0), the ME coupling coefficient α_{ME} decreases to 0, thereby complying with the aforementioned conclusion. It should be noted that for ME coupling coefficient α_{ME}, a certain deviation between results by the FVDAM model and experimental data is observed as no consideration of the influence of factors including contact stress and accurately realizing experimental environment in numerical model on ME coupling coefficient. When the prestress was 0 MPa, the ME coupling coefficient seems especially apt to be affected by the above factors, thus a large deviation between results by the

develop FVDAM model and the experimental data are observed. However, the maximum coupling coefficient and magnetostrictive strain by the FVDAM model are in good agreement with the experimental results, which indicates the validity of the proposed model. This demonstrates that the FVDAM model offers a reliable and promising tool for accurately predicting the nonlinear response of ME composites.

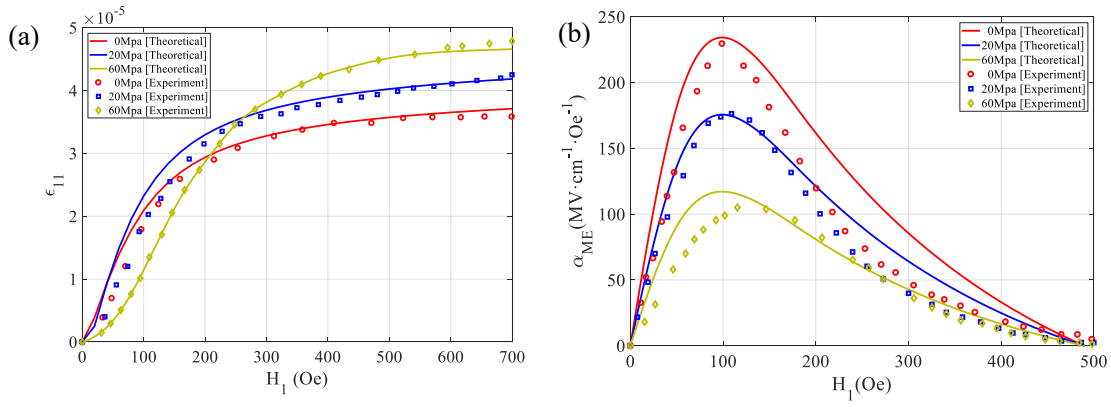

Fig. 5. Comparison of experimental results and theoretical results (a) Magnetostrictive strain ε_{11} and (b) ME coefficient α_{ME} .

4.2. Local field distribution study of magnetic properties

The representative volume element (RVE) is applied to perform the discrete parametric modelling, which enables the FVDAM model to determine local distributions of physical fields and offer an effective numerical tool for assessing the effect of microscopic damage on macroscopic equivalent performance. To verify the convergence of numerical models with different meshes, studies are conducted to analyze the magnetic field and flux distributions using the mesh sizes of 48×48 and 96×96, respectively. A magnetic field loading ($H_2=1000$ Oe) is applied on the boundary of RVE along the transversal direction in the developed FVDAM model. The magnetic field intensity (H_2 , H_3) and magnetic flux density (B_2, B_3) with different mesh configurations are shown in Figs. 6 and 7, respectively. These fields in the vicinity of the magnetostrictive phase exhibit the symmetric pattern with the highest intensity regions (highlighted in red) and lowest intensity regions (highlighted in blue). The overall profiles of the magnetic field intensity distribution and the magnetic flux distribution are similar, indicating a strong correlation between these two field distributions. It is noted that the numerical differences in field distributions for the models with two different meshes are remarkable small, indicating that the numerical results converge. This also demonstrates its feasibility for predicting the local field distributions using different sizes of meshes. Therefore, the FVDAM model with 48×48 discretized meshes is adopted for the analysis of local field predictions in this study.

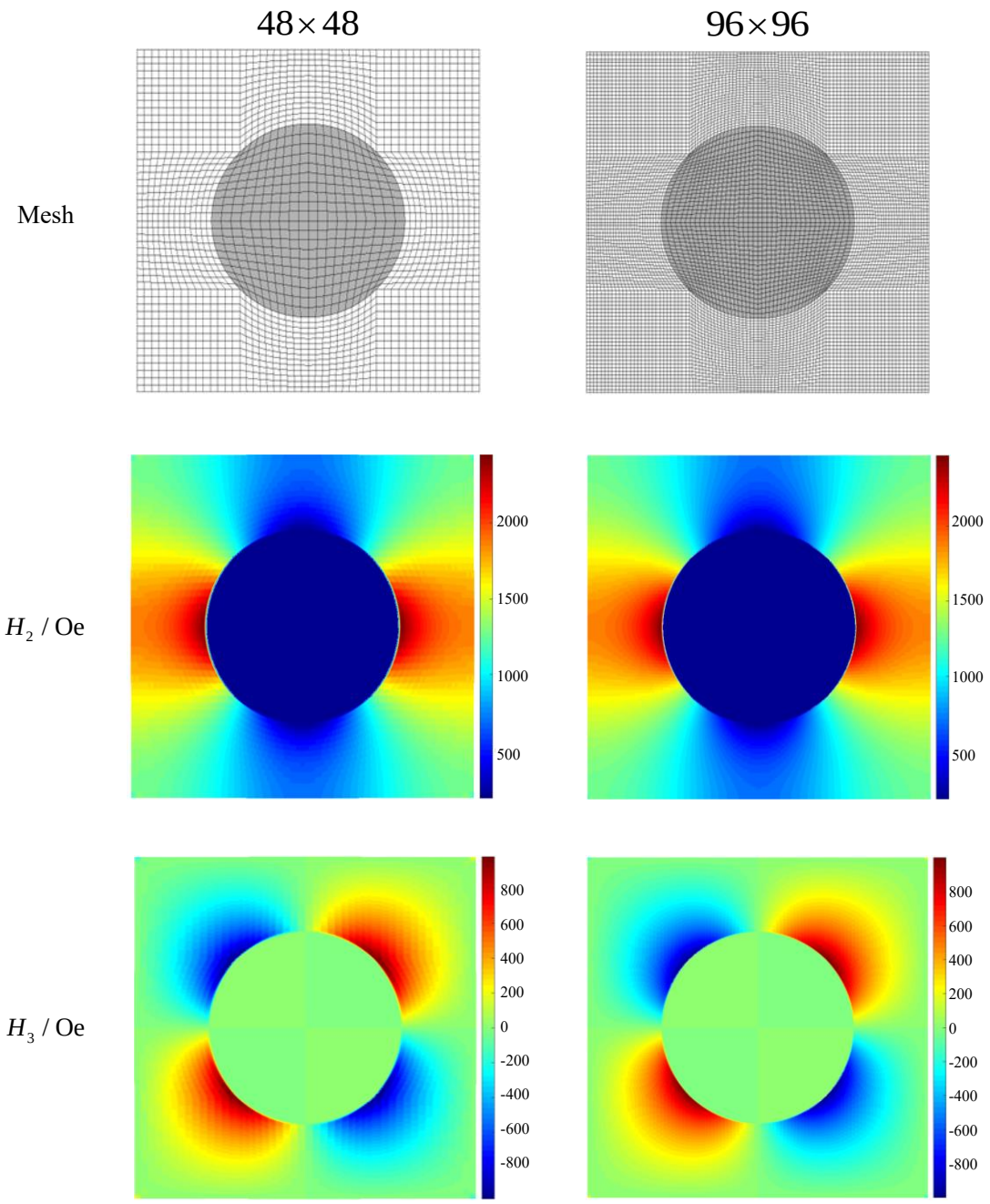

Fig. 6. Comparison of local magnetic field distribution in the sub-cells with mesh sizes of 48×48 and 96×96.

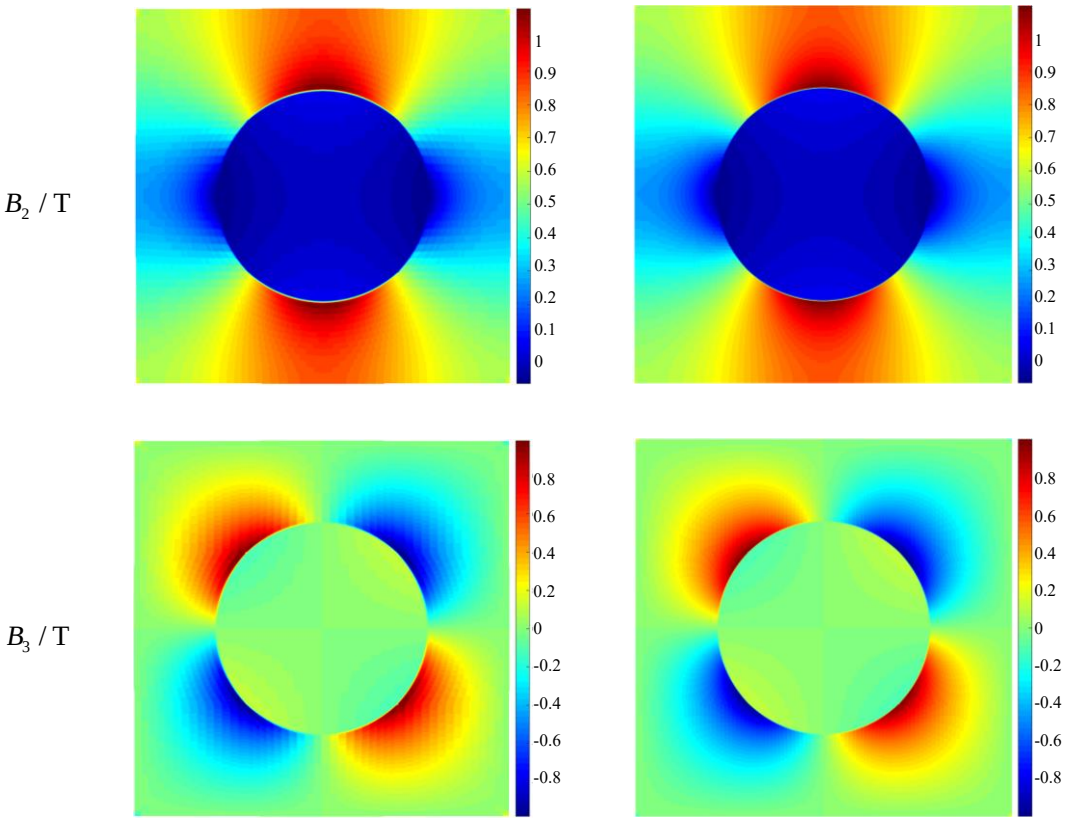

Fig. 7. Comparison of local magnetic flux density distribution in the sub-cells with mesh sizes of 48×48 and 96×96.

4.3. The effect of coupling multi-physics fields on properties of ME composites

In this study, the FVDAM model is utilized to analyze the nonlinear mechanical behavior of ME composites under the multi-physical field environment including the magnetic field, prestress, and temperature. The nonlinear electro-magneto-elastic coupling response is primarily attributed to the magnetization saturation process within the magnetostrictive phase. Fig. 8 shows the nonlinear responses of the magnetization intensity $\mu_0 \bar{M}_1$ and the magnetic flux density $\bar{B}_1$ against an variational magnetic field intensity ($0 \sim 1200$ Oe) under different prestress (i.e., 0 MPa, 20 MPa, 40 MPa, 60 MPa) at the reference temperature $T = 20$ °C . As shown in Fig. 8(a), magnetization gradually approaches saturation with the increase of magnetic field intensity, reaching a maximum saturation magnetization of 0.52 T under a prestress of 60 MPa. The magnetization increases more rapidly with the increase of prestress during the initial magnetization stage (that is to say, when the magnetic field intensity $H_1 \le 400$ Oe). However, the saturation magnetization remains the same value across all four prestress levels (i.e., 0 MPa, 20 MPa, 40 MPa and 60 MPa), indicating that the external loading can only accelerate the magnetization process and has minimal impact on saturation magnetization. Based on Maxwell principle, the magnetic flux density $B_1 = \mu_0 \left(M_1 + H_1 \right)$ depends

on the magnetization intensity M_1 and magnetic field intensity H_1. Therefore, as shown in Fig. 8(b), as the magnetization intensity approaches saturation, the change in the magnetic flux density no longer exhibits the nonlinear behavior. However, the trend in magnetic flux density remains similar under four prestress loads. Overall, the higher levels of prestress significantly enhance the magnetization intensity and magnetic flux density, while its influence diminishes as the magnetization intensity approaches saturation.

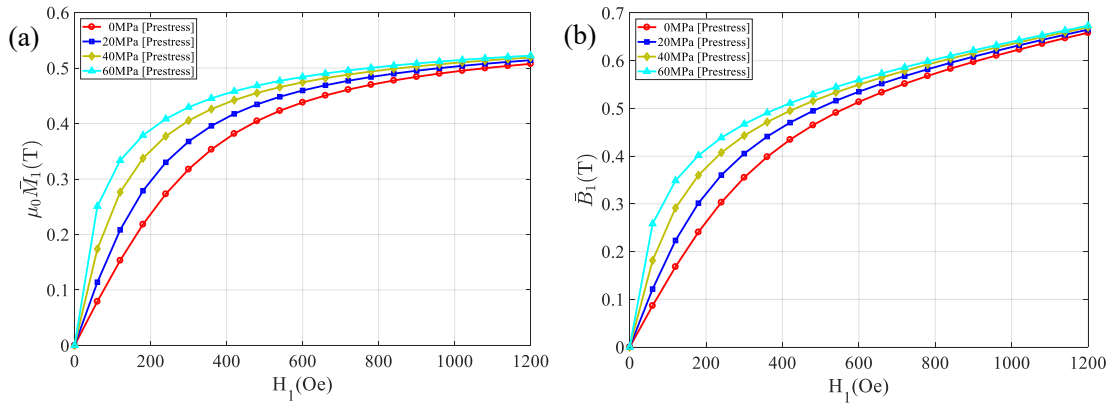

Fig. 8. Nonlinear responses with respect to the magnetic field intensity H_1 under different prestresses at reference temperature $T = 20$ °C (a) Magnetization intensity $\mu_0\bar{M}_1$, and (b) Axial magnetic flux density $\bar{B}_1$.

As the magnetic field intensity increases, internal defects and stresses are reduced due to the rearrangement of magnetic domains within the magnetostrictive material, leading to the changes in the elastic modulus. Applying the FVDAM micromechanical model, the results of the equivalent elastic modulus as a function of the magnetic field intensity ($0 \sim 1000$ Oe) under different prestress loads are shown in Fig. 9. It is noted that the increase of the magnetic field intensity causes the nonlinear change in the elastic modulus, due to the hysteresis on the effect of magnetostriction. With the increase of the applied magnetic field intensity in Fig. 9(a), the equivalent axial elastic modulus E_{11}^* increases, while the equivalent transverse elastic modulus E_{22}^* decreases. The increase of prestress also leads to the increase of the change rate of elastic modulus. Considering a prestress load of 60 MPa, the axial elastic moduli E_{11}^* and transverse elastic moduli E_{22}^* reach the maximum and minimum values of 53.42 GPa and 35.68 GPa, respectively.

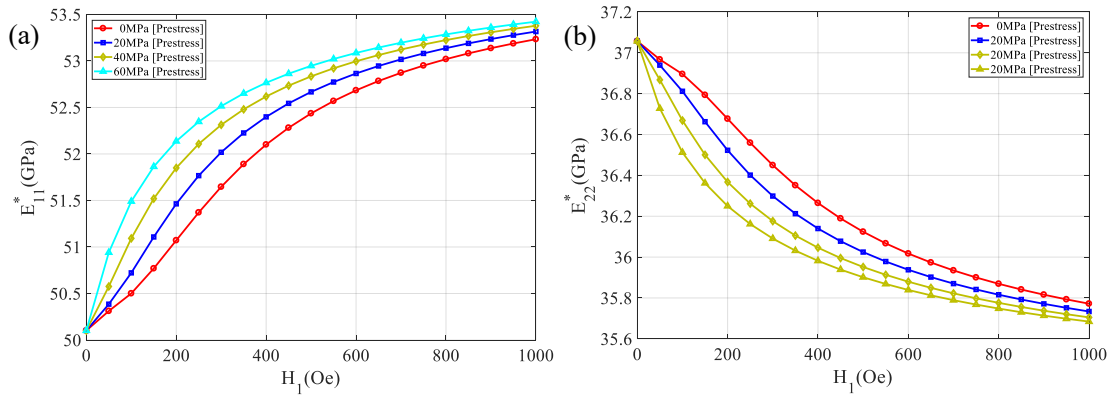

Fig. 9. Comparisons of the equivalent elastic modulus with respect to the magnetic field intensity H_1 under different prestresses at reference temperature $T = 20$ ℃ (a) Axial elastic modulus E_{11}^*, and (b) Transverse elastic moduli E_{22}^*.

Subsequently, Fig. 10 shows the relationship between the equivalent piezomagnetic coefficients of the ME composite and the applied magnetic field intensities under different prestresses. It is worth noting that both the axial stress $\bar{\sigma}_{11}$ and the transverse stress $\bar{\sigma}_{22}$ exhibit significant nonlinear behaviors with the increase of magnetic field intensity. As the magnetization process reaches saturation, the axial and transverse stresses reach maximum values of 1124 MPa and 308 MPa, respectively. In Fig. 10(c), the increase of average electric field intensity $\bar{E}_1$ shows the larger amplitudes under different prestresses. This owes to the electric field intensity $\bar{E}_1$ comes from the piezoelectric effect generated by the interaction of the piezoelectric phase. The strain required to produce the piezoelectric effect includes the internal magnetostrictive strain and the elastic strain of the material generated by the external prestress, which results in a larger amplitude of variation in electric field intensity. Fig. 10(d) illustrates the variation of the equivalent piezomagnetic coefficient q_{11}^* in terms of the magnetic field intensity. The piezomagnetic coefficients q_{11}^* under the four prestress conditions (i.e., 0 MPa, 20 MPa, 40 MPa, 60 MPa) rapidly reach to the peak values (i.e., 110 Pa/Oe, 161 Pa/Oe, 189 Pa/Oe, 219 Pa/Oe) at the initial stage of magnetization, respectively. Then, they quickly decreased to zeros, indicating that the prestress has significant impact on the peak location and magnitude of the piezomagnetic coefficient.

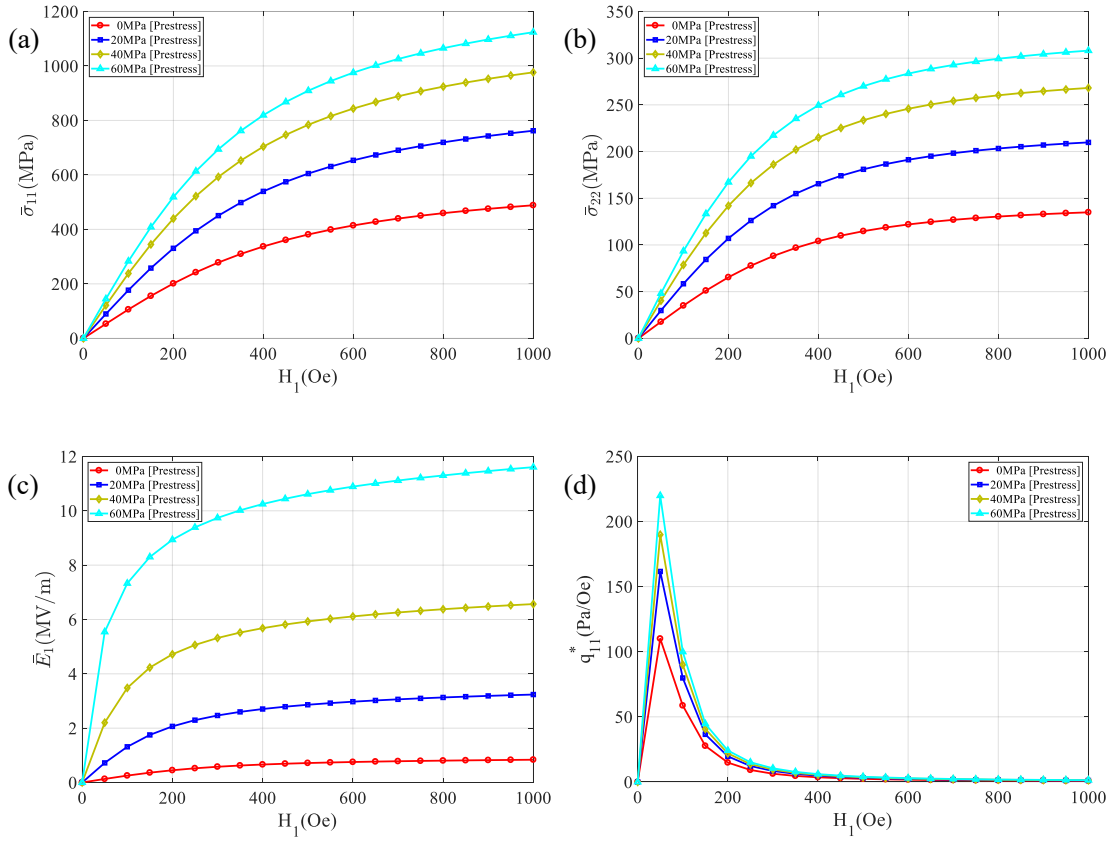

Fig. 10. The distributions of nonlinear responses and equivalent piezomagnetic coefficient with respect to the magnetic field intensity H_1 under different prestresses at reference temperature $T = 20°C$ (a) Axial average stress $\bar{\sigma}_{11}$, (b) Transverse average stress $\bar{\sigma}_{22}$, (c) Average electric field intensity $\bar{E}_1$ and (d) Equivalent piezomagnetic coefficient q^*_{11}.

Finally, the temperature field, as a critical factor influencing the properties and response of ME composites, is investigated using the FVDAM model. Fig. 11 demonstrates the relationship between nonlinear responses and the magnetic field at different temperatures (i.e., 20 °C, 40 °C, 60 °C, 80 °C). To emphasize the impact of temperature on performance of the magnetoelectric composite, no prestress load condition is imposed. On the basis of nonlinear magneto-elastic-thermal constitutive relation in Eq. (10), the residual thermal stress caused by the increased temperature constrains the magnetostrictive stress. Consequently, the magnetostrictive stress responses ($\bar{\sigma}_{11}, \bar{\sigma}_{22}$) are more pronounced at lower temperatures as shown in Figs. 11(a) and (b). With the increase of magnetic field, thermal disturbances induced by the increased temperature impedes the process of magnetization, leading to a weakening of internal stresses. This observation agrees well with the microscopic mechanism of magnetic domain structure. Moreover, as the prestress is not applied in this study, the electric field intensity $\bar{E}_1$ generated by the piezoelectric phase only depends on the variation of the internal stress. Compared to the electric field intensity shown in Fig. 10(c), the electric field intensity in Fig. 11(c) is less influenced by temperature. In Fig. 11(d), the peak value of the equivalent piezomagnetic coefficients q^*_{11} for the magnetic field intensity H_1 in the range of

0 to 200 Oe is significantly affected by temperature, reaching a maximum peak of 110 Pa/Oe at a temperature $T = 20$ °C. While at high magnetic field intensity, the piezomagnetic coefficients q_{11}^{*} at all temperatures tend to be the same value.

Fig. 12 shows the 3D surface plots of the ME coupling coefficients α_{ME} as a function of the magnetic field intensity or the prestress at different ambient temperatures, respectively. Multi-field loading conditions are simulated under the conditions of the magnetic field intensity in the range of 0 to 1000 Oe, prestress between 10 MPa and 60 MPa, and temperature in the range of 20 °C to 100 °C. The decrease of the ME coupling coefficient α_{ME} is observed as the temperature increases. Furthermore, the ME coupling coefficient exhibits a nonlinear relationship with the magnetic field intensity and a linear proportion to prestress. In practical applications, ME composites inevitably work under the condition of high temperature. Simulation results in Fig. 12(b) demonstrate that the increased prestress can compromise the impact of the rising temperature on the ME coupling coefficient, benefiting ME composites for a wide range of applications.

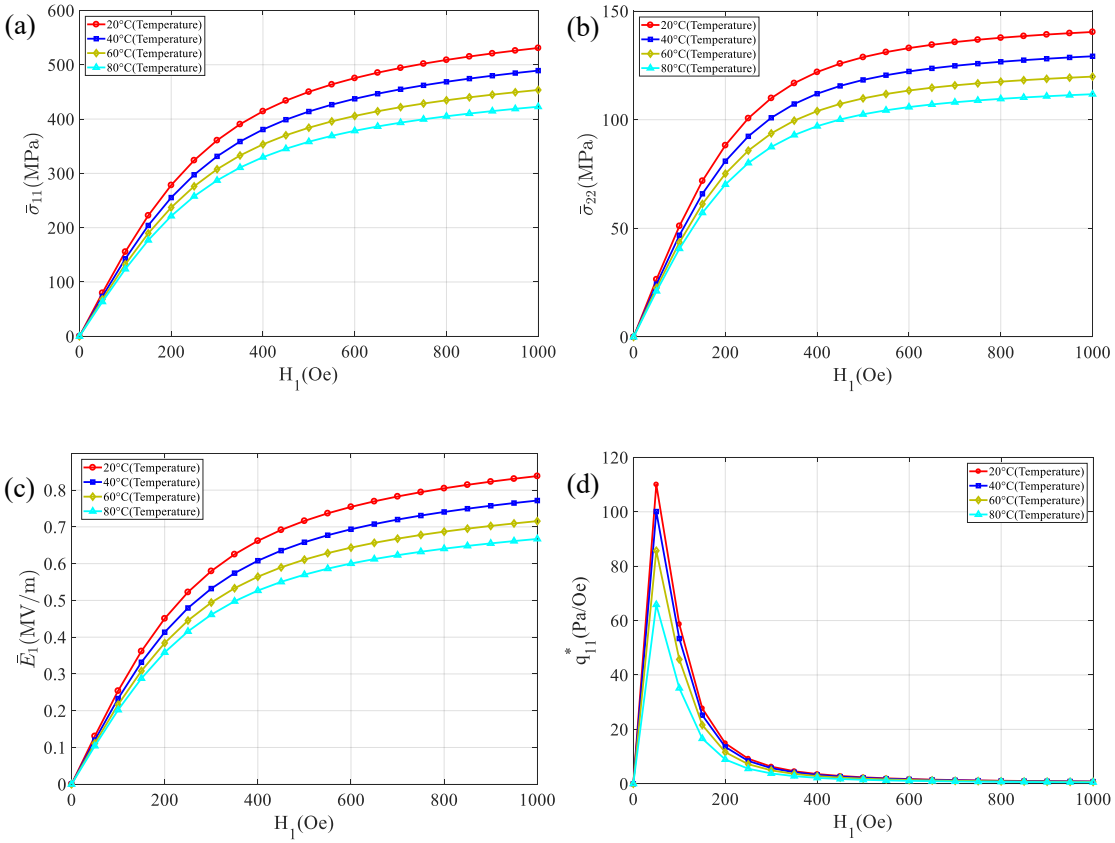

Fig. 11. The distributions of the nonlinear responses with respect to the magnetic field intensity H_1 at temperature $T = 20 \sim 80$ °C (a) Axial average stress $\bar{\sigma}_{11}$, (b) Transverse average stress $\bar{\sigma}_{22}$, (c) Average electric field intensity $\bar{E}_2$ and (d) Equivalent piezomagnetic coefficient q_{11}^{*}.

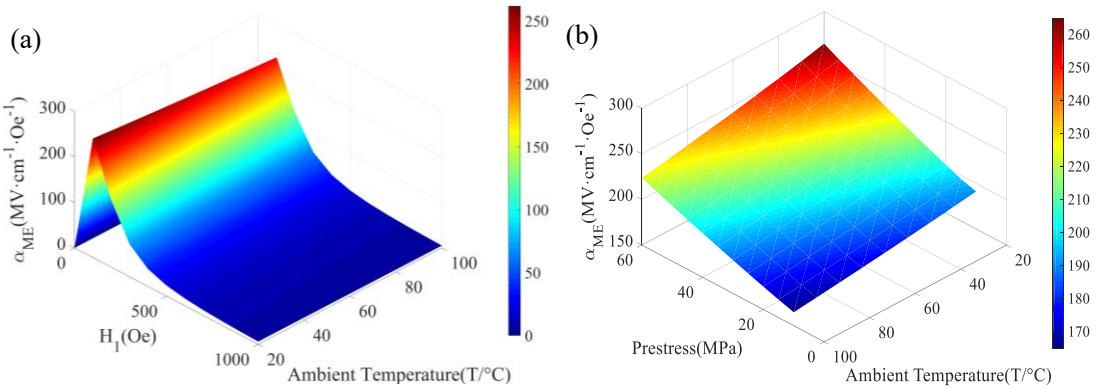

Fig. 12. Surface plots of the ME coupling coefficients combined multi-physics field loadings (a) Magnetic field intensity combined with temperature, and (b) Prestress combined with temperature.

4.4. The effect of local damage on responses of ME composites

The magnetostrictive phase typically consists of ferromagnetic materials, which are more susceptible to cracking and other forms of initial damage due to brittle characteristics. Therefore, it is crucial to analyze the impact of local damage on material properties and mechanical responses using the developed FVDAM model. Fig. 13 shows the stress distribution of the ME composites with different volume fractions ($V_f = 0.25,\ 0.4,\ 0.5$) in the magnetostrictive phase under a magnetic field intensity $H_1 = 1000$ Oe. The material parameters of the pre-set damaged sub-cells are assumed a scale of 0.001 for the magnetostrictive phase (Nickel) in Table 1. The volume fraction of initial damaged sub-cells is set to 0.69%. As the volume fraction of the magnetostrictive phase increases, the initial damage in the sub-cells increases proportionally shown in Fig. 13(a). It is evident that the magnetostrictive stresses concentrate at the edges of the damaged region. With the expansion of the damaged regions, the stress distribution becomes increasingly concentrated and complex, potentially leading to further damage or failure of the material in these areas. The axial stress σ_{11}, aligned with the magnetic field direction, approaches zero within the damaged region shown in Fig. 13(b), indicating the performance degradation in damaged sub-cells. The maximum transverse stress $\sigma_{22}^{\max}$ shown in Fig. 13(c) occurs at the damage interface with values of 272.3 MPa, 291.7 MPa and 334.2 MPa from left to right, respectively. While the maximum shear stress $\sigma_{23}^{\max}$ of different volume fractions remains relatively consistent, its distribution is concentrated around the damaged region, as shown in Fig. 13(d).

Figs. 14(a) and (b) show the relationship between the elastic modulus and volume fraction in the range of 0.1 to 0.6. In order to demonstrate effects of the initial damage on the macroscopic properties, results of the magnetoelectric composite are compared in both the normal and the damaged states. It is noted that the axial elastic modulus E_{11}^{*} increases linearly with the increase of

the volume fraction of the magnetostrictive phase, while the transverse elastic modulus E_{22}^{*} exhibits a nonlinear increase. Moreover, effects of the initial damage on the axial elastic modulus are minor, while the transverse elastic modulus in the damaged area is significantly lower than that in the undamaged region, especially when the volume fraction of magnetostrictive phase increases.

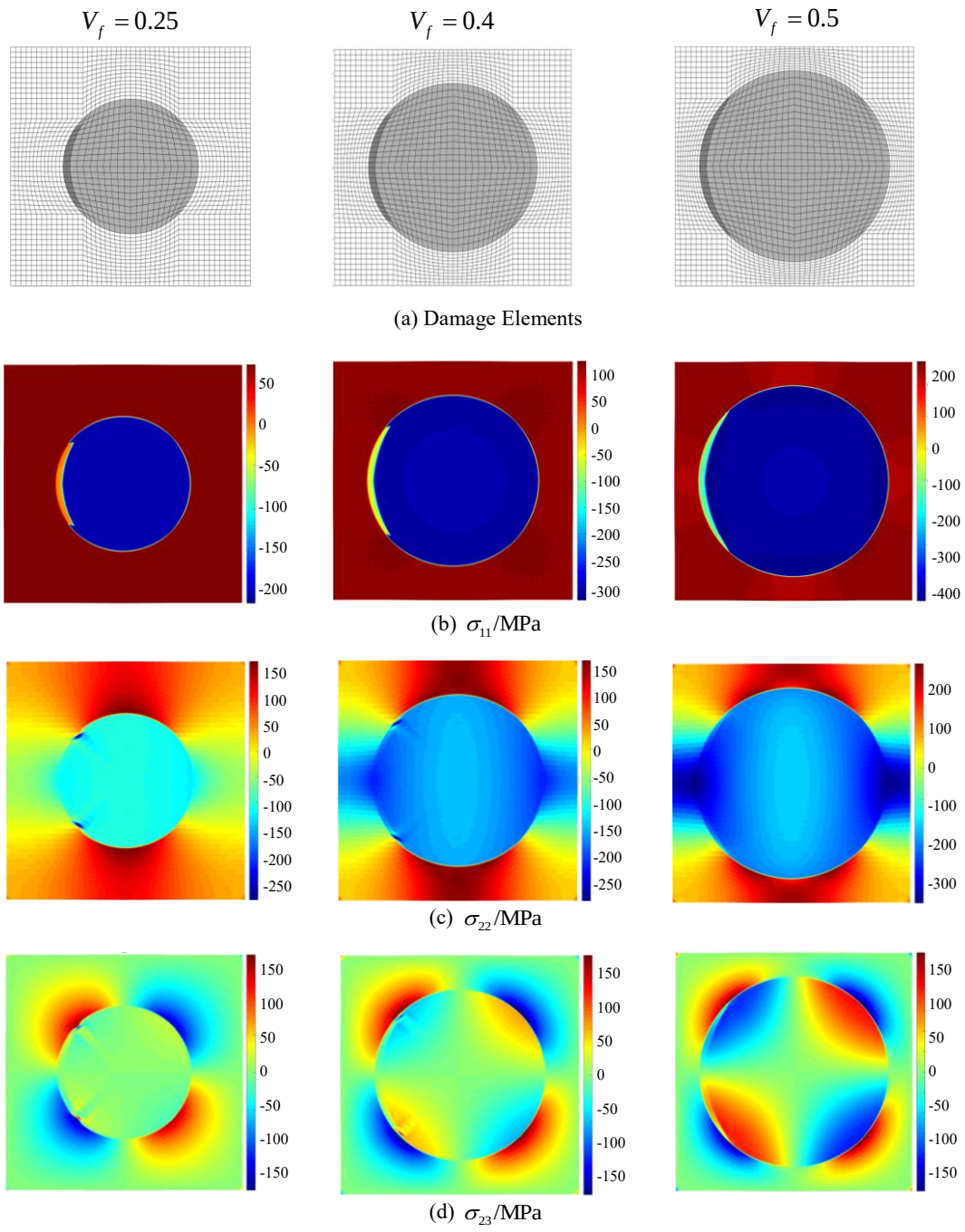

Fig. 13. Distribution of the stress with different volume fractions with 0.25, 0.4 and 0.5 of the magnetostrictive phase at the initial damage state respectively.

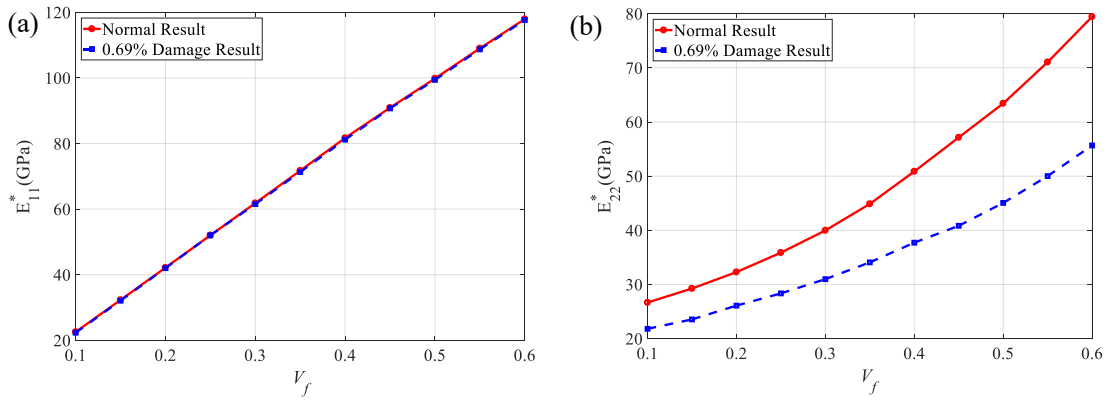

Fig. 14. The variation of elastic modulus with respect to the volume fraction $V_f = 0.1 \sim 0.6$ at the initial damage state and normal state (a) axial elastic modulus E_{11}^*, and (b) transverse elastic modulus E_{22}^*.

In Fig. 15, effects of the volume fraction and initial damage on the piezoelectric coefficients e_{11}^* and ME coupling coefficients α_{ME} are discussed. The increase in the volume fraction of the magnetostrictive phase is accompanied by a corresponding decrease in the volume fraction of the piezoelectric phase, resulting in a linear decrease in the piezoelectric coefficient e_{11}^*, as shown in Fig. 15(a). The piezoelectric coefficient e_{11}^* under damaged conditions closely aligns with the results obtained in the undamaged state, which is attributed to the less weakness of the piezoelectric polymers in the initial damage, as compared to the magnetostrictive materials. The ME coupling coefficient α_{ME} represents the superposition of responses of the magnetostrictive phase and piezoelectric phase. Thus, the ME coupling coefficient α_{ME} exhibits a step-shape change as a function of the volume fraction, as shown in Fig. 15(b). Its peak value is obtained at a specific volume fraction $V_f = 0.3$, while either an excessive or insufficient volume fraction of the magnetostrictive phase leads to a reduced magnitude of ME coupling coefficient. Initial damage leads to a slight reduction in the ME coupling coefficient, but the overall trend remains similar to the result obtained in undamaged state. The peak values under the damaged and undamaged conditions are 285.2 MV · cm^{-1} · Oe^{-1} and 301.3 MV · cm^{-1} · Oe^{-1}, respectively. It is noted that the maximum change in the ME coupling coefficients occurs as the damage state is approximately 5.34%.

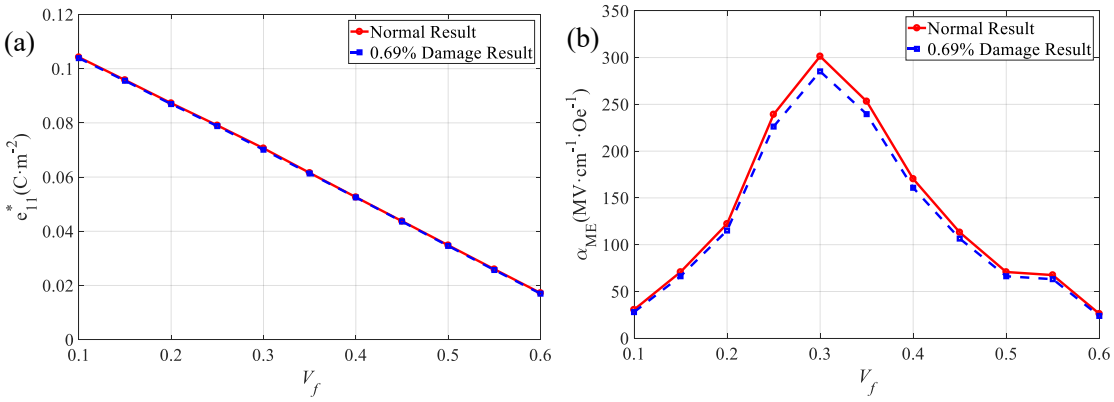

Fig. 15. The variation of the magnetoelectric properties with respect to the volume fraction $V_f = 0.1 \sim 0.6$ under initial damage state and normal state (a) piezoelectric coefficients e_{11}^*, and (b) ME coupling coefficients α_{ME}.

5. Conclusions

In this study, an improved micromechanical modeling framework is developed to conduct nonlinear analysis of magnetoelectric (ME) composites under the fully coupled multi-physics condition. Based on free energy theory, nonlinear electro-magneto-thermo-elastic constitutive relations are derived and then, the representative volume element (RVE) is selected for the parametric discretization with the assumption of periodic boundary conditions. The accuracy of the proposed model is verified by the existing experimental data. Main findings are summarized as follows:

1) Under the influence of magnetic fields, the reorganization of magnetic domains caused by magnetostriction reduces the internal stress, enhancing material stiffness and increasing elasticity modulus. Due to the hysteresis of magnetostriction, the change in elasticity modulus exhibits nonlinear behaviors, and then stabilizes as the magnetization saturates.
2) At the low magnetic field intensities, the increased prestress accelerates the magnetic domain reorganization and enhances the magnetostriction effect, therefore increasing the piezomagnetic coefficients. Once the magnetic field intensity reaches saturation, the magnetic domain configuration stabilizes, and then the piezomagnetic coefficients are reduced by a further increase of the magnetic field intensity.
3) The nonlinear electro-magneto-thermo-elastic constitutive relations show that residual thermal stress from the temperature change inhibits the magnetostriction effect, particularly at low magnetic field intensity. Under high-temperature conditions, both the saturated magnetostriction stress and ME coupling coefficient decrease, though the increased prestress can mitigate these negative effects.
4) Initial damage at the interface leads to stress concentration, potentially causing further failure in this region. The ME coupling coefficients are affected by the interaction between the magnetostrictive and piezoelectric phases, thereby the optimal volume fraction for

maximizing the ME coupling coefficients can be determined by tailoring phase proportions. Summarily, the aforementioned observations provide key information to unveil the performance mechanism of ME composites and lay a solid foundation of understanding for nonlinear behaviors of ME composites under multi-physics field coupling conditions.

Data availability statement

The raw/processed data required to reproduce these findings cannot be shared at this time as the data also forms part of an ongoing study.

CRediT authorship contribution statement

Ziwei Li: Writing-original draft, Methodology, Visualization. **Junjie Ye:** Writing-original draft, Methodology, Conceptualization. **Lu Liu**: Validation, Data curation. **Yiwei Wang:** Visualization, Methodology. **Yang Li**: Resources, Data curation. **Yang Shi**: Methodology, Visualization, Data curation. **Dianzi Liu:** Methodology, Conceptualization, Writing-review & editing, Supervision.

Declaration of Competing Interest

The authors declare that they have no known competing financial interests or personal relationships that could have appeared to influence the work reported in this paper.

Acknowledgments

This work was supported by the National Natural Science Foundation of China, China (No. 52175112). The 111 Project, China (No. B14042).

Appendix

In this Section, the first- and second-order intermediate variables $\Delta W_{(01)}^{(\beta,\gamma)}$, $\Delta W_{(10)}^{(\beta,\gamma)}$, $\Delta W_{(02)}^{(\beta,\gamma)}$ and $\Delta W_{(20)}^{(\beta,\gamma)}$ are eliminated employing the local equilibrium equation in Eqs. (51)-(53), that is,

$$\begin{aligned}
&\left[C_{66}\left(\hat{J}_{22}\right)^2+C_{55}\left(\hat{J}_{32}\right)^2+\left(C_{65}+C_{56}\right)\hat{J}_{22}\hat{J}_{32}\right]W_{1(20)}+\left[C_{66}\left(\hat{J}_{23}\right)^2+C_{55}\left(\hat{J}_{33}\right)^2+\left(C_{65}+C_{56}\right)\hat{J}_{23}\hat{J}_{33}\right]W_{1(02)}+\\
&\left[C_{62}\left(\hat{J}_{22}\right)^2+C_{54}\left(\hat{J}_{32}\right)^2+\left(C_{64}+C_{52}\right)\hat{J}_{22}\hat{J}_{32}\right]W_{2(20)}+\left[C_{62}\left(\hat{J}_{23}\right)^2+C_{54}\left(\hat{J}_{33}\right)^2+\left(C_{64}+C_{52}\right)\hat{J}_{23}\hat{J}_{33}\right]W_{2(02)}+\\
&\left[C_{64}\left(\hat{J}_{22}\right)^2+C_{53}\left(\hat{J}_{32}\right)^2+\left(C_{63}+C_{54}\right)\hat{J}_{22}\hat{J}_{32}\right]W_{3(20)}+\left[C_{64}\left(\hat{J}_{23}\right)^2+C_{53}\left(\hat{J}_{33}\right)^2+\left(C_{63}+C_{54}\right)\hat{J}_{23}\hat{J}_{33}\right]W_{3(02)}+\\
&\left[e_{26}\left(\hat{J}_{22}\right)^2+e_{35}\left(\hat{J}_{32}\right)^2+\left(e_{25}+e_{36}\right)\hat{J}_{22}\hat{J}_{32}^{(m)}\right]W_{4(20)}+\left[e_{26}\left(\hat{J}_{23}\right)^2+e_{33}\left(\hat{J}_{32}\right)^2+\left(e_{25}+e_{36}\right)\hat{J}_{23}\hat{J}_{33}\right]W_{4(02)}+\\
&\left[q_{26}\left(\hat{J}_{22}\right)^2+q_{35}\left(\hat{J}_{32}\right)^2+\left(q_{25}+q_{36}\right)\hat{J}_{22}\hat{J}_{32}\right]W_{5(20)}+\left[q_{26}\left(\hat{J}_{23}\right)^2+q_{33}\left(\hat{J}_{32}\right)^2+\left(q_{25}+q_{36}\right)\hat{J}_{23}\hat{J}_{33}\right]W_{5(02)}=0
\end{aligned} \tag{A.1}$$

$$\left[C_{26}\left(\hat{J}_{22}\right)^2+C_{45}\left(\hat{J}_{32}\right)^2+\left(C_{25}+C_{46}\right)\hat{J}_{22}\hat{J}_{32}\right]W_{1(20)}+\left[C_{26}\left(\hat{J}_{23}\right)^2+C_{25}\left(\hat{J}_{33}\right)^2+\left(C_{25}+C_{46}\right)\hat{J}_{23}\hat{J}_{33}\right]W_{1(02)}+$$
$$\left[C_{22}\left(\hat{J}_{22}\right)^2+C_{44}\left(\hat{J}_{32}\right)^2+\left(C_{24}+C_{42}\right)\hat{J}_{22}\hat{J}_{32}\right]W_{2(20)}+\left[C_{22}\left(\hat{J}_{23}\right)^2+C_{44}\left(\hat{J}_{33}\right)^2+\left(C_{24}+C_{42}\right)\hat{J}_{23}\hat{J}_{33}\right]W_{2(02)}+$$
$$\left[C_{24}\left(\hat{J}_{22}\right)^2+C_{43}\left(\hat{J}_{32}\right)^2+\left(C_{23}+C_{44}\right)\hat{J}_{22}\hat{J}_{32}\right]W_{3(20)}+\left[C_{24}\left(\hat{J}_{23}\right)^2+C_{43}\left(\hat{J}_{33}\right)^2+\left(C_{23}+C_{44}\right)\hat{J}_{23}\hat{J}_{33}\right]W_{3(02)}+$$
$$\left[e_{22}\left(\hat{J}_{22}\right)^2+e_{34}\left(\hat{J}_{32}\right)^2+\left(e_{24}+e_{32}\right)\hat{J}_{22}\hat{J}_{32}\right]W_{4(20)}+\left[e_{22}\left(\hat{J}_{23}\right)^2+e_{34}\left(\hat{J}_{33}\right)^2+\left(e_{24}+e_{32}\right)\hat{J}_{23}\hat{J}_{33}\right]W_{4(02)}+$$
$$\left[q_{22}\left(\hat{J}_{22}\right)^2+q_{34}\left(\hat{J}_{32}\right)^2+\left(q_{24}+q_{32}\right)\hat{J}_{22}\hat{J}_{32}\right]W_{5(20)}+\left[q_{22}\left(\hat{J}_{23}\right)^2+q_{34}\left(\hat{J}_{33}\right)^2+\left(q_{24}+q_{32}\right)\hat{J}_{23}\hat{J}_{33}\right]W_{5(02)}=0 \tag{A.2}$$

$$\left[C_{46}\left(\hat{J}_{22}\right)^2+C_{35}\left(\hat{J}_{32}\right)^2+\left(C_{45}+C_{36}\right)\hat{J}_{22}\hat{J}_{32}\right]W_{1(20)}+\left[C_{46}\left(\hat{J}_{23}\right)^2+C_{35}\left(\hat{J}_{33}\right)^2+\left(C_{45}+C_{36}\right)\hat{J}_{23}\hat{J}_{33}\right]W_{1(02)}+$$
$$\left[C_{42}\left(\hat{J}_{22}\right)^2+C_{34}\left(\hat{J}_{32}\right)^2+\left(C_{44}+C_{32}\right)\hat{J}_{22}\hat{J}_{32}\right]W_{2(20)}+\left[C_{42}\left(\hat{J}_{23}\right)^2+C_{34}\left(\hat{J}_{33}\right)^2+\left(C_{44}+C_{32}\right)\hat{J}_{23}\hat{J}_{33}\right]W_{2(02)}+$$
$$\left[C_{44}\left(\hat{J}_{22}\right)^2+C_{33}\left(\hat{J}_{32}\right)^2+\left(C_{43}+C_{34}\right)\hat{J}_{22}\hat{J}_{32}\right]W_{3(20)}+\left[C_{44}\left(\hat{J}_{23}\right)^2+C_{33}\left(\hat{J}_{33}\right)^2+\left(C_{43}+C_{34}\right)\hat{J}_{23}\hat{J}_{33}\right]W_{3(02)}+$$
$$\left[e_{24}\left(\hat{J}_{22}\right)^2+e_{35}\left(\hat{J}_{32}\right)^2+\left(e_{23}+e_{34}\right)\hat{J}_{22}\hat{J}_{32}\right]W_{4(20)}+\left[e_{24}\left(\hat{J}_{23}\right)^2+e_{35}\left(\hat{J}_{33}\right)^2+\left(e_{23}+e_{34}\right)\hat{J}_{23}\hat{J}_{33}\right]W_{4(02)}+$$
$$\left[q_{24}\left(\hat{J}_{22}\right)^2+q_{35}\left(\hat{J}_{32}\right)^2+\left(q_{23}+q_{34}\right)\hat{J}_{22}\hat{J}_{32}\right]W_{5(20)}+\left[q_{24}\left(\hat{J}_{23}\right)^2+q_{35}\left(\hat{J}_{33}\right)^2+\left(q_{23}+q_{34}\right)\hat{J}_{23}\hat{J}_{33}\right]W_{5(02)}=0 \tag{A.3}$$

$$\left[e_{26}\left(\hat{J}_{22}\right)^2+e_{35}\left(\hat{J}_{32}\right)^2+\left(e_{25}+e_{36}\right)\hat{J}_{22}\hat{J}_{32}\right]W_{1(20)}+\left[e_{26}\left(\hat{J}_{23}\right)^2+e_{35}\left(\hat{J}_{33}\right)^2+\left(e_{25}+e_{36}\right)\hat{J}_{23}\hat{J}_{33}\right]W_{1(02)}+$$
$$\left[e_{22}\left(\hat{J}_{22}\right)^2+e_{34}\left(\hat{J}_{32}\right)^2+\left(e_{24}+e_{32}\right)\hat{J}_{22}\hat{J}_{32}\right]W_{2(20)}+\left[e_{22}\left(\hat{J}_{23}\right)^2+e_{34}\left(\hat{J}_{33}\right)^2+\left(e_{24}+e_{32}\right)\hat{J}_{23}\hat{J}_{33}\right]W_{2(02)}+$$
$$\left[e_{24}\left(\hat{J}_{22}\right)^2+e_{33}\left(\hat{J}_{32}\right)^2+\left(e_{23}+e_{34}\right)\hat{J}_{22}\hat{J}_{32}\right]W_{3(20)}+\left[e_{24}\left(\hat{J}_{23}\right)^2+e_{33}\left(\hat{J}_{33}\right)^2+\left(e_{23}+e_{34}\right)\hat{J}_{23}\hat{J}_{33}\right]W_{3(02)}-$$
$$\left[\kappa_{22}\left(\hat{J}_{22}\right)^2+\kappa_{33}\left(\hat{J}_{32}\right)^2+\left(\kappa_{23}+\kappa_{32}\right)\hat{J}_{22}\hat{J}_{32}\right]W_{4(20)}-\left[\kappa_{22}\left(\hat{J}_{23}\right)^2+\kappa_{33}\left(\hat{J}_{33}\right)^2+\left(\kappa_{23}+\kappa_{32}\right)\hat{J}_{23}\hat{J}_{33}\right]W_{4(02)}-$$
$$\left[\alpha_{22}\left(\hat{J}_{22}\right)^2+\alpha_{33}\left(\hat{J}_{32}\right)^2+\left(\alpha_{23}+\alpha_{32}\right)\hat{J}_{22}\hat{J}_{32}\right]W_{5(20)}-\left[\alpha_{22}\left(\hat{J}_{23}\right)^2+\alpha_{33}\left(\hat{J}_{33}\right)^2+\left(\alpha_{23}+\alpha_{32}\right)\hat{J}_{23}\hat{J}_{33}\right]W_{5(02)}=0 \tag{A.4}$$

$$\left[q_{26}\left(\hat{J}_{22}\right)^2+q_{35}\left(\hat{J}_{32}\right)^2+\left(q_{25}+q_{36}\right)\hat{J}_{22}\hat{J}_{32}\right]W_{1(20)}+\left[q_{26}\left(\hat{J}_{23}\right)^2+q_{35}\left(\hat{J}_{33}\right)^2+\left(q_{25}+q_{36}\right)\hat{J}_{23}\hat{J}_{33}\right]W_{1(02)}+$$
$$\left[q_{22}\left(\hat{J}_{22}\right)^2+q_{34}\left(\hat{J}_{32}\right)^2+\left(q_{24}+q_{32}\right)\hat{J}_{22}\hat{J}_{32}\right]W_{2(20)}+\left[q_{22}\left(\hat{J}_{23}\right)^2+q_{34}\left(\hat{J}_{33}\right)^2+\left(q_{24}+q_{32}\right)\hat{J}_{23}\hat{J}_{33}\right]W_{2(02)}+$$
$$\left[q_{24}\left(\hat{J}_{22}\right)^2+q_{33}\left(\hat{J}_{32}\right)^2+\left(q_{23}+q_{34}\right)\hat{J}_{22}\hat{J}_{32}\right]W_{3(20)}+\left[q_{24}\left(\hat{J}_{23}\right)^2+q_{33}\left(\hat{J}_{33}\right)^2+\left(q_{23}+q_{34}\right)\hat{J}_{23}\hat{J}_{33}\right]W_{3(02)}-$$
$$\left[\alpha_{22}\left(\hat{J}_{22}\right)^2+\alpha_{33}\left(\hat{J}_{32}\right)^2+\left(\alpha_{23}+\alpha_{32}\right)\hat{J}_{22}\hat{J}_{32}\right]W_{4(20)}-\left[\alpha_{22}\left(\hat{J}_{23}\right)^2+\alpha_{33}\left(\hat{J}_{33}\right)^2+\left(\alpha_{23}+\alpha_{32}\right)\hat{J}_{23}\hat{J}_{33}\right]W_{4(02)}-$$
$$\left[\mu_{22}\left(\hat{J}_{22}\right)^2+\mu_{33}\left(\hat{J}_{32}\right)^2+\left(\mu_{23}+\mu_{32}\right)\hat{J}_{22}\hat{J}_{32}\right]W_{5(20)}-\left[\mu_{22}\left(\hat{J}_{23}\right)^2+\mu_{33}\left(\hat{J}_{33}\right)^2+\left(\mu_{23}+\mu_{32}\right)\hat{J}_{23}\hat{J}_{33}\right]W_{5(02)}=0 \tag{A.5}$$

The zero-order intermediate variable $\Delta W_{(00)}^{(\alpha,\beta)}$ is expressed in matrix form as a function of the surface-averaged displacement, potential, and magnetic potential, as follows:

$$
\begin{aligned}
L_{11} &= C_{55}\left[\left(\hat{J}_{32}\right)^2+\left(\hat{J}_{33}\right)^2\right]+C_{66}\left[\left(\hat{J}_{22}\right)^2+\left(\hat{J}_{23}\right)^2\right]+\left(C_{56}+C_{65}\right)\left(\hat{J}_{22}\hat{J}_{32}+\hat{J}_{23}\hat{J}_{33}\right)\\
L_{12} &= C_{54}\left[\left(\hat{J}_{32}\right)^2+\left(\hat{J}_{33}\right)^2\right]+C_{62}\left[\left(\hat{J}_{22}\right)^2+\left(\hat{J}_{23}\right)^2\right]+\left(C_{52}+C_{64}\right)\left(\hat{J}_{22}\hat{J}_{32}+\hat{J}_{23}\hat{J}_{33}\right)\\
L_{13} &= C_{53}\left[\left(\hat{J}_{32}\right)^2+\left(\hat{J}_{33}\right)^2\right]+C_{64}\left[\left(\hat{J}_{22}\right)^2+\left(\hat{J}_{23}\right)^2\right]+\left(C_{54}+C_{63}\right)\left(\hat{J}_{22}\hat{J}_{32}+\hat{J}_{23}\hat{J}_{33}\right)\\
L_{14} &= e_{35}\left[\left(\hat{J}_{32}\right)^2+\left(\hat{J}_{33}\right)^2\right]+e_{26}\left[\left(\hat{J}_{22}\right)^2+\left(\hat{J}_{23}\right)^2\right]+\left(e_{25}+e_{36}\right)\left(\hat{J}_{22}\hat{J}_{32}+\hat{J}_{23}\hat{J}_{33}\right)\\
L_{15} &= q_{35}\left[\left(\hat{J}_{32}\right)^2+\left(\hat{J}_{33}\right)^2\right]+q_{26}\left[\left(\hat{J}_{22}\right)^2+\left(\hat{J}_{23}\right)^2\right]+\left(q_{25}+q_{36}\right)\left(\hat{J}_{22}\hat{J}_{32}+\hat{J}_{23}\hat{J}_{33}\right)
\end{aligned}
\tag{A.6}
$$

$$
\begin{aligned}
L_{21} &= C_{45}\left[\left(\hat{J}_{32}\right)^2+\left(\hat{J}_{33}\right)^2\right]+C_{26}\left[\left(\hat{J}_{22}\right)^2+\left(\hat{J}_{23}\right)^2\right]+\left(C_{46}+C_{25}\right)\left(\hat{J}_{22}\hat{J}_{32}+\hat{J}_{23}\hat{J}_{33}\right)\\
L_{22} &= C_{44}\left[\left(\hat{J}_{32}\right)^2+\left(\hat{J}_{33}\right)^2\right]+C_{22}\left[\left(\hat{J}_{22}\right)^2+\left(\hat{J}_{23}\right)^2\right]+\left(C_{42}+C_{24}\right)\left(\hat{J}_{22}\hat{J}_{32}+\hat{J}_{23}\hat{J}_{33}\right)\\
L_{23} &= C_{43}\left[\left(\hat{J}_{32}\right)^2+\left(\hat{J}_{33}\right)^2\right]+C_{24}\left[\left(\hat{J}_{22}\right)^2+\left(\hat{J}_{23}\right)^2\right]+\left(C_{44}+C_{23}\right)\left(\hat{J}_{22}\hat{J}_{32}+\hat{J}_{23}\hat{J}_{33}\right)\\
L_{24} &= e_{34}\left[\left(\hat{J}_{32}\right)^2+\left(\hat{J}_{33}\right)^2\right]+e_{22}\left[\left(\hat{J}_{22}\right)^2+\left(\hat{J}_{23}\right)^2\right]+\left(e_{24}+e_{32}\right)\left(\hat{J}_{22}\hat{J}_{32}+\hat{J}_{23}\hat{J}_{33}\right)\\
L_{25} &= q_{34}\left[\left(\hat{J}_{32}\right)^2+\left(\hat{J}_{33}\right)^2\right]+q_{22}\left[\left(\hat{J}_{22}\right)^2+\left(\hat{J}_{23}\right)^2\right]+\left(q_{24}+q_{32}\right)\left(\hat{J}_{22}\hat{J}_{32}+\hat{J}_{23}\hat{J}_{33}\right)
\end{aligned}
\tag{A.7}
$$

$$
\begin{aligned}
L_{31} &= C_{35}\left[\left(\hat{J}_{32}\right)^2+\left(\hat{J}_{33}\right)^2\right]+C_{46}\left[\left(\hat{J}_{22}\right)^2+\left(\hat{J}_{23}\right)^2\right]+\left(C_{36}+C_{45}\right)\left(\hat{J}_{22}\hat{J}_{32}+\hat{J}_{23}\hat{J}_{33}\right)\\
L_{32} &= C_{34}\left[\left(\hat{J}_{32}\right)^2+\left(\hat{J}_{33}\right)^2\right]+C_{42}\left[\left(\hat{J}_{22}\right)^2+\left(\hat{J}_{23}\right)^2\right]+\left(C_{32}+C_{44}\right)\left(\hat{J}_{22}\hat{J}_{32}+\hat{J}_{23}\hat{J}_{33}\right)\\
L_{33} &= C_{33}\left[\left(\hat{J}_{32}\right)^2+\left(\hat{J}_{33}\right)^2\right]+C_{44}\left[\left(\hat{J}_{22}\right)^2+\left(\hat{J}_{23}\right)^2\right]+\left(C_{34}+C_{43}\right)\left(\hat{J}_{22}\hat{J}_{32}+\hat{J}_{23}\hat{J}_{33}\right)\\
L_{34} &= e_{35}\left[\left(\hat{J}_{32}\right)^2+\left(\hat{J}_{33}\right)^2\right]+e_{24}\left[\left(\hat{J}_{22}\right)^2+\left(\hat{J}_{23}\right)^2\right]+\left(e_{23}+e_{34}\right)\left(\hat{J}_{22}\hat{J}_{32}+\hat{J}_{23}\hat{J}_{33}\right)\\
L_{35} &= q_{35}\left[\left(\hat{J}_{32}\right)^2+\left(\hat{J}_{33}\right)^2\right]+q_{24}\left[\left(\hat{J}_{22}\right)^2+\left(\hat{J}_{23}\right)^2\right]+\left(q_{23}+q_{34}\right)\left(\hat{J}_{22}\hat{J}_{32}+\hat{J}_{23}\hat{J}_{33}\right)
\end{aligned}
\tag{A.8}
$$

$$
\begin{aligned}
L_{41} &= e_{35}\left[\left(\hat{J}_{32}\right)^2+\left(\hat{J}_{33}\right)^2\right]+e_{26}\left[\left(\hat{J}_{22}\right)^2+\left(\hat{J}_{23}\right)^2\right]+\left(e_{36}+e_{25}\right)\left(\hat{J}_{22}\hat{J}_{32}+\hat{J}_{23}\hat{J}_{33}\right)\\
L_{42} &= e_{34}\left[\left(\hat{J}_{32}\right)^2+\left(\hat{J}_{33}\right)^2\right]+e_{22}\left[\left(\hat{J}_{22}\right)^2+\left(\hat{J}_{23}\right)^2\right]+\left(e_{32}+e_{24}\right)\left(\hat{J}_{22}\hat{J}_{32}+\hat{J}_{23}\hat{J}_{33}\right)\\
L_{43} &= e_{33}\left[\left(\hat{J}_{32}\right)^2+\left(\hat{J}_{33}\right)^2\right]+e_{24}\left[\left(\hat{J}_{22}\right)^2+\left(\hat{J}_{23}\right)^2\right]+\left(e_{34}+e_{23}\right)\left(\hat{J}_{22}\hat{J}_{32}+\hat{J}_{23}\hat{J}_{33}\right)\\
L_{44} &= -\kappa_{33}\left[\left(\hat{J}_{32}\right)^2+\left(\hat{J}_{33}\right)^2\right]-\kappa_{22}\left[\left(\hat{J}_{22}\right)^2+\left(\hat{J}_{23}\right)^2\right]-\left(\kappa_{32}+\kappa_{23}\right)\left(\hat{J}_{22}\hat{J}_{32}+\hat{J}_{23}\hat{J}_{33}\right)\\
L_{45} &= -\alpha_{33}\left[\left(\hat{J}_{32}\right)^2+\left(\hat{J}_{33}\right)^2\right]-\alpha_{22}\left[\left(\hat{J}_{22}\right)^2+\left(\hat{J}_{23}\right)^2\right]-\left(\alpha_{32}+\alpha_{23}\right)\left(\hat{J}_{22}\hat{J}_{32}+\hat{J}_{23}\hat{J}_{33}\right)
\end{aligned}
\tag{A.9}
$$

$$
\begin{aligned}
L_{51} &= q_{35}\left[\left(\hat{J}_{32}\right)^2+\left(\hat{J}_{33}\right)^2\right]+q_{26}\left[\left(\hat{J}_{22}\right)^2+\left(\hat{J}_{23}\right)^2\right]+\left(q_{36}+q_{25}\right)\left(\hat{J}_{22}\hat{J}_{32}+\hat{J}_{23}\hat{J}_{33}\right)\\
L_{52} &= q_{34}\left[\left(\hat{J}_{32}\right)^2+\left(\hat{J}_{33}\right)^2\right]+q_{22}\left[\left(\hat{J}_{22}\right)^2+\left(\hat{J}_{23}\right)^2\right]+\left(q_{32}+q_{24}\right)\left(\hat{J}_{22}\hat{J}_{32}+\hat{J}_{23}\hat{J}_{33}\right)\\
L_{53} &= q_{33}\left[\left(\hat{J}_{32}\right)^2+\left(\hat{J}_{33}\right)^2\right]+q_{24}\left[\left(\hat{J}_{22}\right)^2+\left(\hat{J}_{23}\right)^2\right]+\left(q_{34}+q_{23}\right)\left(\hat{J}_{22}\hat{J}_{32}+\hat{J}_{23}\hat{J}_{33}\right)\\
L_{54} &= -\alpha_{33}\left[\left(\hat{J}_{32}\right)^2+\left(\hat{J}_{33}\right)^2\right]-\alpha_{22}\left[\left(\hat{J}_{22}\right)^2+\left(\hat{J}_{23}\right)^2\right]-\left(\alpha_{32}+\alpha_{23}\right)\left(\hat{J}_{22}\hat{J}_{32}+\hat{J}_{23}\hat{J}_{33}\right)\\
L_{55} &= -\mu_{33}\left[\left(\hat{J}_{32}\right)^2+\left(\hat{J}_{33}\right)^2\right]-\mu_{22}\left[\left(\hat{J}_{22}\right)^2+\left(\hat{J}_{23}\right)^2\right]-\left(\mu_{32}+\mu_{23}\right)\left(\hat{J}_{22}\hat{J}_{32}+\hat{J}_{23}\hat{J}_{33}\right)
\end{aligned}
\tag{A.10}
$$

$$
R_{11}=\frac{C_{55}\hat{J}_{32}+C_{66}\hat{J}_{22}+\hat{J}_{22}\hat{J}_{32}\left(C_{56}+C_{65}\right)}{2},\ R_{12}=\frac{C_{55}\hat{J}_{33}+C_{66}\hat{J}_{23}+\hat{J}_{23}\hat{J}_{33}\left(C_{56}+C_{65}\right)}{2} \tag{A.11}
$$

$$
R_{13}=\frac{C_{54}\hat{J}_{32}+C_{62}\hat{J}_{22}+\hat{J}_{22}\hat{J}_{32}\left(C_{52}+C_{64}\right)}{2},\ R_{14}=\frac{C_{54}\hat{J}_{33}+C_{62}\hat{J}_{23}+\hat{J}_{23}\hat{J}_{33}\left(C_{52}+C_{64}\right)}{2} \tag{A.12}
$$

$$
R_{15}=\frac{C_{53}\hat{J}_{32}+C_{64}\hat{J}_{22}+\hat{J}_{22}\hat{J}_{32}\left(C_{54}+C_{63}\right)}{2},\ R_{16}=\frac{C_{53}\hat{J}_{33}+C_{64}\hat{J}_{23}+\hat{J}_{23}\hat{J}_{33}\left(C_{54}+C_{63}\right)}{2} \tag{A.13}
$$

$$
R_{17}=\frac{e_{35}\hat{J}_{32}+e_{26}\hat{J}_{22}+\hat{J}_{22}\hat{J}_{32}\left(e_{25}+e_{36}\right)}{2},\ R_{18}=\frac{e_{35}\hat{J}_{33}+e_{26}\hat{J}_{23}+\hat{J}_{23}\hat{J}_{33}\left(e_{25}+e_{36}\right)}{2} \tag{A.14}
$$

$$
R_{19}=\frac{q_{35}\hat{J}_{32}+q_{26}\hat{J}_{22}+\hat{J}_{22}\hat{J}_{32}\left(q_{25}+q_{36}\right)}{2},\ R_{110}=\frac{q_{35}\hat{J}_{33}+q_{26}\hat{J}_{23}+\hat{J}_{23}\hat{J}_{33}\left(q_{25}+q_{36}\right)}{2} \tag{A.15}
$$

$$
R_{21}=\frac{C_{45}\hat{J}_{32}+C_{26}\hat{J}_{22}+\hat{J}_{22}\hat{J}_{32}\left(C_{46}+C_{25}\right)}{2},\ R_{22}=\frac{C_{45}\hat{J}_{33}+C_{26}\hat{J}_{23}+\hat{J}_{23}\hat{J}_{33}\left(C_{46}+C_{25}\right)}{2} \tag{A.16}
$$

$$
R_{23}=\frac{C_{44}\hat{J}_{32}+C_{22}\hat{J}_{22}+\hat{J}_{22}\hat{J}_{32}\left(C_{42}+C_{24}\right)}{2},\ R_{24}=\frac{C_{44}\hat{J}_{33}+C_{22}\hat{J}_{23}+\hat{J}_{23}\hat{J}_{33}\left(C_{42}+C_{24}\right)}{2} \tag{A.17}
$$

$$
R_{25}=\frac{C_{43}\hat{J}_{32}+C_{24}\hat{J}_{22}+\hat{J}_{22}\hat{J}_{32}\left(C_{44}+C_{23}\right)}{2},\ R_{26}=\frac{C_{43}\hat{J}_{33}+C_{24}\hat{J}_{23}+\hat{J}_{23}\hat{J}_{33}\left(C_{44}+C_{23}\right)}{2} \tag{A.18}
$$

$$
R_{25}=\frac{C_{43}\hat{J}_{32}+C_{24}\hat{J}_{22}+\hat{J}_{22}\hat{J}_{32}\left(C_{44}+C_{23}\right)}{2},\ R_{26}=\frac{C_{43}\hat{J}_{33}+C_{24}\hat{J}_{23}+\hat{J}_{23}\hat{J}_{33}\left(C_{44}+C_{23}\right)}{2} \tag{A.19}
$$

$$
R_{27}=\frac{e_{34}\hat{J}_{32}+e_{22}\hat{J}_{22}+\hat{J}_{22}\hat{J}_{32}\left(e_{24}+e_{32}\right)}{2},\ R_{28}=\frac{e_{34}\hat{J}_{33}+e_{22}\hat{J}_{23}+\hat{J}_{23}\hat{J}_{33}\left(e_{24}+e_{32}\right)}{2} \tag{A.20}
$$

$$
R_{29}=\frac{q_{34}\hat{J}_{32}+q_{22}\hat{J}_{22}+\hat{J}_{22}\hat{J}_{32}\left(q_{24}+q_{32}\right)}{2},\ R_{210}=\frac{q_{34}\hat{J}_{33}+q_{22}\hat{J}_{23}+\hat{J}_{23}\hat{J}_{33}\left(q_{24}+q_{32}\right)}{2} \tag{A.21}
$$

$$R_{31}=\frac{C_{35}\hat{J}_{32}+C_{46}\hat{J}_{22}+\hat{J}_{22}\hat{J}_{32}\left(C_{36}+C_{45}\right)}{2},\ R_{32}=\frac{C_{35}\hat{J}_{33}+C_{46}\hat{J}_{23}+\hat{J}_{23}\hat{J}_{33}\left(C_{36}+C_{45}\right)}{2} \tag{A.22}$$

$$R_{33}=\frac{C_{34}\hat{J}_{32}+C_{42}\hat{J}_{22}+\hat{J}_{22}\hat{J}_{32}\left(C_{32}+C_{44}\right)}{2},\ R_{34}=\frac{C_{34}\hat{J}_{33}+C_{42}\hat{J}_{23}+\hat{J}_{23}\hat{J}_{33}\left(C_{32}+C_{44}\right)}{2} \tag{A.23}$$

$$R_{35}=\frac{C_{33}\hat{J}_{32}+C_{44}\hat{J}_{22}+\hat{J}_{22}\hat{J}_{32}\left(C_{34}+C_{43}\right)}{2},\ R_{36}=\frac{C_{33}\hat{J}_{33}+C_{44}\hat{J}_{23}+\hat{J}_{23}\hat{J}_{33}\left(C_{34}+C_{43}\right)}{2} \tag{A.24}$$

$$R_{37}=\frac{e_{35}\hat{J}_{32}+e_{24}\hat{J}_{22}+\hat{J}_{22}\hat{J}_{32}\left(e_{23}+e_{34}\right)}{2},\ R_{38}=\frac{e_{35}\hat{J}_{33}+e_{24}\hat{J}_{23}+\hat{J}_{23}\hat{J}_{33}\left(e_{23}+e_{34}\right)}{2} \tag{A.25}$$

$$R_{39}=\frac{q_{35}\hat{J}_{32}+q_{24}\hat{J}_{22}+\hat{J}_{22}\hat{J}_{32}\left(q_{23}+q_{34}\right)}{2},\ R_{310}=\frac{q_{35}\hat{J}_{33}+q_{24}\hat{J}_{23}+\hat{J}_{23}\hat{J}_{33}\left(q_{23}+q_{34}\right)}{2} \tag{A.26}$$

$$R_{41}=\frac{e_{35}\hat{J}_{32}+e_{26}\hat{J}_{22}+\hat{J}_{22}\hat{J}_{32}\left(e_{36}+e_{25}\right)}{2},\ R_{42}=\frac{e_{35}\hat{J}_{33}+e_{26}\hat{J}_{23}+\hat{J}_{23}\hat{J}_{33}\left(e_{36}+e_{25}\right)}{2} \tag{A.27}$$

$$R_{43}=\frac{e_{34}\hat{J}_{32}+e_{22}\hat{J}_{22}+\hat{J}_{22}\hat{J}_{32}\left(e_{32}+e_{24}\right)}{2},\ R_{44}=\frac{e_{34}\hat{J}_{33}+e_{22}\hat{J}_{23}+\hat{J}_{23}\hat{J}_{33}\left(e_{32}+e_{24}\right)}{2} \tag{A.28}$$

$$R_{45}=\frac{e_{33}\hat{J}_{32}+e_{24}\hat{J}_{22}+\hat{J}_{22}\hat{J}_{32}\left(e_{34}+e_{23}\right)}{2},\ R_{46}=\frac{e_{33}\hat{J}_{33}+e_{24}\hat{J}_{23}+\hat{J}_{23}\hat{J}_{33}\left(e_{34}+e_{23}\right)}{2} \tag{A.29}$$

$$R_{47}=-\frac{\kappa_{33}\hat{J}_{32}+\kappa_{22}\hat{J}_{22}+\hat{J}_{22}\hat{J}_{32}\left(\kappa_{32}+\kappa_{23}\right)}{2},\ R_{48}=-\frac{\kappa_{33}\hat{J}_{33}+\kappa_{22}\hat{J}_{23}+\hat{J}_{23}\hat{J}_{33}\left(\kappa_{32}+\kappa_{23}\right)}{2} \tag{A.30}$$

$$R_{49}=-\frac{\alpha_{33}\hat{J}_{32}+\alpha_{22}\hat{J}_{22}+\hat{J}_{22}\hat{J}_{32}\left(\alpha_{32}+\alpha_{23}\right)}{2},\ R_{410}=-\frac{\alpha_{33}\hat{J}_{33}+\alpha_{22}\hat{J}_{23}+\hat{J}_{23}\hat{J}_{33}\left(\alpha_{32}+\alpha_{23}\right)}{2} \tag{A.31}$$

$$R_{51}=\frac{q_{35}\hat{J}_{32}+q_{26}\hat{J}_{22}+\hat{J}_{22}\hat{J}_{32}\left(q_{36}+q_{25}\right)}{2},\ R_{52}=\frac{q_{35}\hat{J}_{33}+q_{26}\hat{J}_{23}+\hat{J}_{23}\hat{J}_{33}\left(q_{36}+q_{25}\right)}{2} \tag{A.32}$$

$$R_{53}=\frac{q_{34}\hat{J}_{32}+q_{22}\hat{J}_{22}+\hat{J}_{22}\hat{J}_{32}\left(q_{32}+q_{24}\right)}{2},\ R_{54}=\frac{q_{34}\hat{J}_{33}+q_{22}\hat{J}_{23}+\hat{J}_{23}\hat{J}_{33}\left(q_{32}+q_{24}\right)}{2} \tag{A.33}$$

$$R_{55}=\frac{q_{33}\hat{J}_{32}+q_{24}\hat{J}_{22}+\hat{J}_{22}\hat{J}_{32}\left(q_{34}+q_{23}\right)}{2},\ R_{56}=\frac{q_{33}\hat{J}_{33}+q_{24}\hat{J}_{23}+\hat{J}_{23}\hat{J}_{33}\left(q_{34}+q_{23}\right)}{2} \tag{A.34}$$

$$R_{57}=-\frac{\alpha_{33}\hat{J}_{32}+\alpha_{22}\hat{J}_{22}+\hat{J}_{22}\hat{J}_{32}\left(\alpha_{32}+\alpha_{23}\right)}{2},\ R_{58}=-\frac{\alpha_{33}\hat{J}_{33}+\alpha_{22}\hat{J}_{23}+\hat{J}_{23}\hat{J}_{33}\left(\alpha_{32}+\alpha_{23}\right)}{2} \tag{A.35}$$

$$R_{59} = -\frac{\mu_{33}\hat{J}_{32} + \mu_{22}\hat{J}_{22} + \hat{J}_{22}\hat{J}_{32}\left(\mu_{32} + \mu_{23}\right)}{2},\ R_{510} = -\frac{\mu_{33}\hat{J}_{33} + \mu_{22}\hat{J}_{23} + \hat{J}_{23}\hat{J}_{33}\left(\mu_{32} + \mu_{23}\right)}{2} \quad \text{(A.36)}$$

References

[1] Yao Z, Wang YE, Keller S, Carman GP. Bulk Acoustic Wave-Mediated Multiferroic Antennas: Architecture and Performance Bound. IEEE Trans Antennas Propag 2015;63:3335–44. https://doi.org/10.1109/TAP.2015.2431723.

[2] Reermann J, Durdaut P, Salzer S, Demming T, Piorra A, Quandt E, et al.. Evaluation of magnetoelectric sensor systems for cardiological applications. Meas J Int Meas Confed 2018;116:230–8. https://doi.org/10.1016/j.measurement.2017.09.047.

[3] Kopyl S, Surmenev R, Surmeneva M, Fetisov Y, Kholkin A. Magnetoelectric effect: principles and applications in biology and medicine– a review. Mater Today Bio 2021;12:100149. https://doi.org/10.1016/j.mtbio.2021.100149.

[4] Cheng Y, Peng B, Hu Z, Zhou Z, Liu M. Recent development and status of magnetoelectric materials and devices. Phys Lett Sect A Gen At Solid State Phys 2018;382:3018–25. https://doi.org/10.1016/j.physleta.2018.07.014.

[5] Ramesh R, Spaldin NA. Multiferroics: Progress and prospects in thin films. Nanosci Technol A Collect Rev from Nat Journals 2009;3:20–8. https://doi.org/10.1142/9789814287005_0003.

[6] Milenkovic S, Slavkovic V, Fragassa C, Grujovic N, Palic N, Zivic F. Effect of the raster orientation on strength of the continuous fiber reinforced PVDF/PLA composites, fabricated by hand-layup and fused deposition modeling. Compos Struct 2021;270:114063. https://doi.org/10.1016/j.compstruct.2021.114063.

[7] Liu S, Zou H, Qin B, Huang S, Deng L. Tailored magnetoelectric coupling in magnetically oriented polymer-based iron fiber composite. J Magn Magn Mater 2021;540:168408. https://doi.org/10.1016/j.jmmm.2021.168408.

[8] Qi Y, Yao C, Xu H, Zhang J, Weng GJ. Phase-field simulations on the frequency-dependent evolution of nano-magnetic domains and hysteresis loops of ferromagnetic Terfenol-D. Mater Today Commun 2022;32:103849. https://doi.org/10.1016/j.mtcomm.2022.103849.

[9] Newacheck S, Youssef G. Synthesis and characterization of polarized novel 0–3 Terfenol-D/PVDF-TrFE composites. Compos Part B Eng 2019;172:97–102. https://doi.org/10.1016/j.compositesb.2019.05.043.

[10] Kuo HY, Peng CY. Magnetoelectricity in coated fibrous composites of piezoelectric and piezomagnetic phases. Int J Eng Sci 2013;62:70–83. https://doi.org/10.1016/j.ijengsci.2012.08.002.

[11] Espinosa-Almeyda Y, Camacho-Montes H, Otero JA, Rodríguez-Ramos R, López-Realpozo JC, Guinovart-Díaz R, et al.. Interphase effect on the effective magneto-electro-elastic properties for three-phase fiber-reinforced composites by a semi-analytical approach. Int J Eng Sci 2020;154. https://doi.org/10.1016/j.ijengsci.2020.103310.

[12] Ghidini M, Mansell R, Maccherozzi F, Moya X, Phillips LC, Yan W, et al.. Shear-strain-mediated magnetoelectric effects revealed by imaging. Nat Mater 2019;18:840–5. https://doi.org/10.1038/s41563-019-0374-8.

[13] Ma J, Hu J, Li Z, Nan CW. Recent progress in multiferroic magnetoelectric composites: From bulk to thin films. Adv Mater 2011;23:1062–87. https://doi.org/10.1002/adma.201003636.

[14] Srinivasan G, Rasmussen ET, Levin BJ, Hayes R. Magnetoelectric effects in bilayers and multilayers of magnetostrictive and piezoelectric perovskite oxides. Phys Rev B - Condens Matter Mater Phys 2002;65:1–7. https://doi.org/10.1103/PhysRevB.65.134402.

[15] Dong S, Li JF, Viehland D. Characterization of magnetoelectric laminate composites operated in longitudinal-transverse and transverse-transverse modes. J Appl Phys 2004;95:2625–30. https://doi.org/10.1063/1.1644027.

[16] Nersessian N, Or SW, Carman GP. Magneto-thermo-mechanical characterization of 1-3 type polymer-bonded Terfenol-D composites. J Magn Magn Mater 2003;263:101–12. https://doi.org/10.1016/S0304-8853(02)01542-1.

[17] Jiles DC, Thoelke JB. Magnetization and Magnetostriction in Terbium–Dysprosium–Iron Alloys. Phys Status Solidi 1995;147:535–51. https://doi.org/10.1002/pssa.2211470224.

[18] Carman GP, Mitrovic M. Nonlinear Constitutive Relations for Magnetostrictive Materials with Applications to 1-D Problems. J Intell Mater Syst Struct 1994:673–83.

[19] Duenas TA, Hsu L, Carman GP. Magnetostrictive composite material systems analytical/experimental. Mater Res Soc Symp - Proc 1997;459:527–43. https://doi.org/10.1557/proc-459-527.

[20] Zheng XJ, Liu XE. A nonlinear constitutive model for Terfenol-D rods. J Appl Phys 2005;97. https://doi.org/10.1063/1.1850618.

[21] Liu X, Zheng X. Nonlinear constitutive model for magnetostrictive materials. Acta Mech Sin Xuebao 2005;21:278–85. https://doi.org/10.1007/s10409-005-0028-8.

[22] Dinzart F, Sabar H. Magneto-electro-elastic coated inclusion problem and its application to magnetic-piezoelectric composite materials. Int J Solids Struct 2011;48:2393–401. https://doi.org/10.1016/j.ijsolstr.2011.04.010.

[23] Herbst JF, Capehart TW, Pinkerton FE. Estimating the effective magnetostriction of a composite: A simple model. Appl Phys Lett 1997;70:3041–3. https://doi.org/10.1063/1.118743.

[24] Tong ZH, Lo SH, Jiang CP, Cheung YK. An exact solution for the three-phase thermo-electro-magneto-elastic cylinder model and its application to piezoelectric-magnetic fiber composites. Int J Solids Struct 2008;45:5205–19. https://doi.org/10.1016/j.ijsolstr.2008.04.003.

[25] Malakooti MH, Sodano HA. Multi-Inclusion modeling of multiphase piezoelectric composites. Compos Part B Eng 2013;47:181–9. https://doi.org/10.1016/j.compositesb.2012.10.034.

[26] Sladek J, Novak P, Bishay PL, Sladek V. Effective properties of cement-based porous piezoelectric ceramic composites. Constr Build Mater 2018;190:1208–14. https://doi.org/10.1016/j.conbuildmat.2018.09.127.

[27] Govorukha V, Kamlah M, Loboda V, Lapusta Y. Interface cracks in piezoelectric materials. Smart Mater Struct 2016;25. https://doi.org/10.1088/0964-1726/25/2/023001.

[28] Wang X, Zhang J, Xia X, Fang C, Weng GJ. Nonlinear magnetoelectric effects of polymer-based hybrid magnetoelectric composites with chain-like terfenol-D/epoxy and PVDF multilayers. Compos Sci Technol 2021;216:109069. https://doi.org/10.1016/j.compscitech.2021.109069.

[29] Zhang J, Wang X, Chen X, Du H, Weng GJ. Finite element analysis of the magnetoelectric effect on hybrid magnetoelectric composites. Compos Struct 2022;296:115876.

https://doi.org/10.1016/j.compstruct.2022.115876.

[30] Zhou L, Li X, Li M, Żur KK. The smoothed finite element method for time-dependent mechanical responses of MEE materials and structures around Curie temperature. Comput Methods Appl Mech Eng 2020;370. https://doi.org/10.1016/j.cma.2020.113241.

[31] Bansal Y, Pindera MJ. A second look at the higher-order theory for periodic multiphase materials. J Appl Mech Trans ASME 2005;72:177–95. https://doi.org/10.1115/1.1831294.

[32] Bansal Y, Pindera MJ. Finite-volume direct averaging micromechanics of heterogeneous materials with elastic-plastic phases. Int J Plast 2006;22:775–825. https://doi.org/10.1016/j.ijplas.2005.04.012.

[33] Khatam H, Pindera MJ. Parametric finite-volume micromechanics of periodic materials with elastoplastic phases. Int J Plast 2009;25:1386–411. https://doi.org/10.1016/j.ijplas.2008.09.003.

[34] Cavalcante MAA, Marques SPC, Pindera MJ. Parametric formulation of the finite-volume theory for functionally graded materials - Part I: Analysis. J Appl Mech Trans ASME 2007;74:935–45. https://doi.org/10.1115/1.2722312.

[35] Chen Q, Wang G. Homogenized and localized responses of coated magnetostrictive porous materials and structures. Compos Struct 2018;187:102–15. https://doi.org/10.1016/j.compstruct.2017.12.032.

[36] Chen Q, Tu W, Liu R, Chen X. Parametric multiphysics finite-volume theory for periodic composites with thermo-electro-elastic phases. J Intell Mater Syst Struct 2018;29:530–52. https://doi.org/10.1177/1045389X17711789.

[37] Chen Q, Wang G. Computationally-efficient homogenization and localization of unidirectional piezoelectric composites with partially cracked interface. Compos Struct 2020;232:111452. https://doi.org/10.1016/j.compstruct.2019.111452.

[38] Li Z, Ye J, Liu L, Cai H, He WP, Cai G, et al.. Evaluation of piezoelectric and mechanical properties of the piezoelectric composites with local damages. Mech Adv Mater Struct 2022;29:3429–46. https://doi.org/10.1080/15376494.2021.1901322.

[39] Li Z, Ye J, Wang Y, Liu L, Shi Y, Li Y, et al.. A novel micromechanical method for nonlinear analysis of magnetostrictive composites. Compos Struct 2023;311:116633. https://doi.org/10.1016/j.compstruct.2022.116633.

[40] Yu Jiang LI, Dunn ML. Micromechanics of magnetoelectroelastic composite materials: average fields and effective behavior. J Intell Mater Syst Struct 1998;9:404–16. https://doi.org/10.1177/1045389x9800900602.

[41] Charalambakis N. Homogenization techniques and micromechanics. A survey and perspectives. Appl Mech Rev 2010;63:1–10. https://doi.org/10.1115/1.4001911.

[42] He Z, Pindera MJ. Locally exact asymptotic homogenization of periodic materials under anti-plane shear loading. Eur J Mech A/Solids 2020;81:103972. https://doi.org/10.1016/j.euromechsol.2020.103972.

[43] Zhan YS, Lin C hong. Micromechanics-based constitutive modeling of magnetostrictive 1–3 and 0–3 composites. Compos Struct 2021;260:1–16. https://doi.org/10.1016/j.compstruct.2020.113264.

[44] Liu F, Hashim NA, Liu Y, Abed MRM, Li K. Progress in the production and modification of PVDF membranes. J Memb Sci 2011;375:1–27. https://doi.org/10.1016/j.memsci.2011.03.014.

[45] Elakkiya VS, Sudersan S, Arockiarajan A. Stress-dependent nonlinear magnetoelectric effect in press-fit composites: A numerical and experimental study. Eur J Mech A/Solids

2022;93:104536. https://doi.org/10.1016/j.euromechsol.2022.104536.

[46] Koroglu L, Ayas E, Ay N. 3D Printing of Polyvinylidene Fluoride Based Piezoelectric Nanocomposites: An Overview. Macromol Mater Eng 2021;306. https://doi.org/10.1002/mame.202100277.

[47] Yan J, Liu M, Jeong YG, Kang W, Li L, Zhao Y, et al.. Performance enhancements in poly(vinylidene fluoride)-based piezoelectric nanogenerators for efficient energy harvesting. Nano Energy 2019;56:662–92. https://doi.org/10.1016/j.nanoen.2018.12.010.

[48] Chaurasiya A, Pal P, Vas J V., Kumar D, Piramanayagam SN, Singh AK, et al.. Nickel ferrite embedded polyvinylidene fluoride composite based flexible magneto-electric systems. Ceram Int 2020;46:25873–80. https://doi.org/10.1016/j.ceramint.2020.07.070.

[49] Reis S, Silva MP, Castro N, Correia V, Martins P, Lasheras A, et al.. Characterization of Metglas/poly(vinylidene fluoride)/Metglas magnetoelectric laminates for AC/DC magnetic sensor applications. Mater Des 2016;92:906–10. https://doi.org/10.1016/j.matdes.2015.12.086.